6-4-2020 2:00 PM

Cardiac Modelling Techniques to Predict Future Heart Function and New Biomarkers in Acute Myocardial Infarction

Sergio C. H. Dempsey, *The University of Western Ontario*

© Sergio C. H. Dempsey 2020

Recommended Citation

Abstract

Fundamental to treatment planning for patients that have suffered myocardial infarction are predictive biomarkers and risk factors. Important among these in terms of a patient's treatment plan or prognosis are the contractility of the damaged myofibers, final infarct volume, and poor infarct healing rate. Proposed and developed in this thesis are techniques to predict these biomarkers and risk factors using cardiac biomechanical modelling. One of the developed techniques was a CT compatible shape optimization technique which can predict the contraction force of healthy, and stunned myofibers within 6.3% and the distribution of potentially necrotic myofibers within 10% accuracy. The second study involved development of infarct healing network proposed to reduce the complexity of modeling hearts with myocardial infarction while also staging the healing rate and measure collagen concentration in the infarct region reasonably accurately. Finally, an evaluation of how best to measure cardiac output by indicator dilution theory was executed.

Keywords

Summary for Lay Audience

When patients suffer a heart attack, it is important to assess the damage as best as possible to prepare a treatment plan for the patient. During this damage assessment there are many measurements which describe the heart's function in the current state, however, very measurements can predict future heart's function after recovery.

This thesis describes development of a technique for patient specific heart models to predict how the patient's heart will function after it has healed from a heart attack. Specifically, the techniques are designed to predict the range the heart muscle function and its efficiency after healing. This information can be used to predict how much blood the heart will be able to pump in a single heartbeat which is an important measurement used to monitor heart failure.

For the above technique to be accurate, it is important that different regions of the heart (healthy and injured) are modelled correctly. To this end, we introduced a novel technique which requires a very small number of parameters accurately model heart tissue with sustained injury from myocardial infarction. This simplified technique can determine the healing stage of scar tissue and predict the amount of building blocks (microconstituents) of heart tissue in the damaged area. Such information is very useful for diagnosis and it can aid in determining an optimal course of treatment.

The above techniques must be validated in animal studies before use in the clinic. To prepare a future study on animal models, we also improved current techniques to predict blood flow in the heart using CT which is required for damage assessment and modelling validation.

Co-Authorship Statement

This thesis contains materials from two journal paper manuscripts and one conference publication. Neither journal papers are currently submitted, while the conference paper is accepted for publication in EMBC 2020. These articles are included in the following chapters:

Chapter 2: "Characterizing Regional Myofiber Damage Post Acute Myocardial Infarction Using Shape Optimization" by Sergio Dempsey, Aaron So, and Abbas Samani. Aaron So aided in the review process. Abbas Samani was the core contributor to the study design and guidance. He also aided in the review process. I aided in the study design, produced the results and wrote the manuscript.

Chapter 3: "A Composite Material Based Neural Network for Tissue Mechanical Property Estimation Toward Stage Assessment of Infarction" by Sergio Dempsey, Parya Jafari, Aaron So, and Abbas Samani. Parya Jafari helped code the tissue model and produce curve fits. Aaron So aided with the review process. Abbas Samani contributed to the study design, provided guidance and contributed extensively to the review process. I was the core contributor to the study design, processed the results and wrote the manuscript.

Chapter 4: "Cardiac Output Paper" by Sergio Dempsey, Abbas Samani and Aaron So. Abbas Samani aided in the review process. Aaron So was a core contributor in the study design and aided in the review process. I was a core contributor to the study design, processed the results and wrote the manuscript.

Acknowledgments

There are many who have contributed towards helping me complete this thesis. Even before its inception and onward; I thank Abbas Samani for first allowing me into his lab at the end of my 1st year at Western. After taking his course I knew this was a field I wanted to be a part of, and little did I know that by asking to help, and him accepting, a friendship would begin that has led me to where I am now 4.5 years later. During this study Abbas has maintained an encouraging attitude helping me reach my full potential and always keep my mind clinical; something that will be seen throughout this thesis. It's a shame that only in the last few months did I begin to realize it. I look forward to many more discussions and collaboration in the future. Without the slip ups!

I'm thankful to my other supervisor Aaron So for different reasons. In my meetings with Aaron, constant, almost defense like discussions hammered in my understanding of the fundamental assumptions and requirements for the data collection of my thesis and kept me sure of what I was doing.

I'm thankful to all the members who contributed to the collection of pig data for use in Chapter 4.

To my lab members Brett Coelho and Parya Jafari. Our discussions and progress in the lab were an absolute pleasure. When we collaborated, we were researchers to be reckoned with! I trust we'll maintain the same creativity in our respective careers.

Lastly, my thanks go to my wife Taylor. From late nights, early mornings, me constantly walking around talking to myself, and countless stress relieving hugs. Thank you for your support.

<div align="center">

Hic Finis Est

♈ Sergio Dempsey

</div>

Table of Contents

List of Tables

List of Figures

Chapter 1

1 « Introduction »

Cardiovascular disease (CVD) remains the leading cause of death worldwide (Benjamin, 2018). In the case were a CVD leads to acute myocardial infarction (AMI), there is sparsity in available biomarkers to better personalize patient therapy and recovery post revascularization [Chen, 2019]. In this thesis we present two new biomarkers based on cardiac biomechanical modelling which can provide predictive and prognostic value to the clinic.

1.1 « Heart Anatomy and Physiology »

1.1.1 « The Heart »

The heart is the organ that drives the cardiovascular system which is responsible for delivering oxygen and nutrients throughout the entire body (Gray, 2005). Its whole structure is shown in Figure 1-1. The heart is divided into four chambers: left atrium (LA), right atrium (RA), left ventricle (LV) and right ventricle (RV). Each atrium is separated by its respective ventricle by a valve which dictates direction of flow. Each of these valves is connected to a set of papillary muscle inside the ventricles which is used to prevent back flow during contraction. The role of flow is described in Section 1.1.2. There are two other valves separating the ventricles from their respective vasculature termed the pulmonary valve for the RV which leads to the lungs, and the aortic valve which leads to the aorta and artery vasculature which supplies blood to the rest of the body. Lastly, not depicted are the sinoatrial (SA) and atrioventricular (AV) nodes which are the electrical trigger for cardiac contraction which sets the whole cycle in motion.
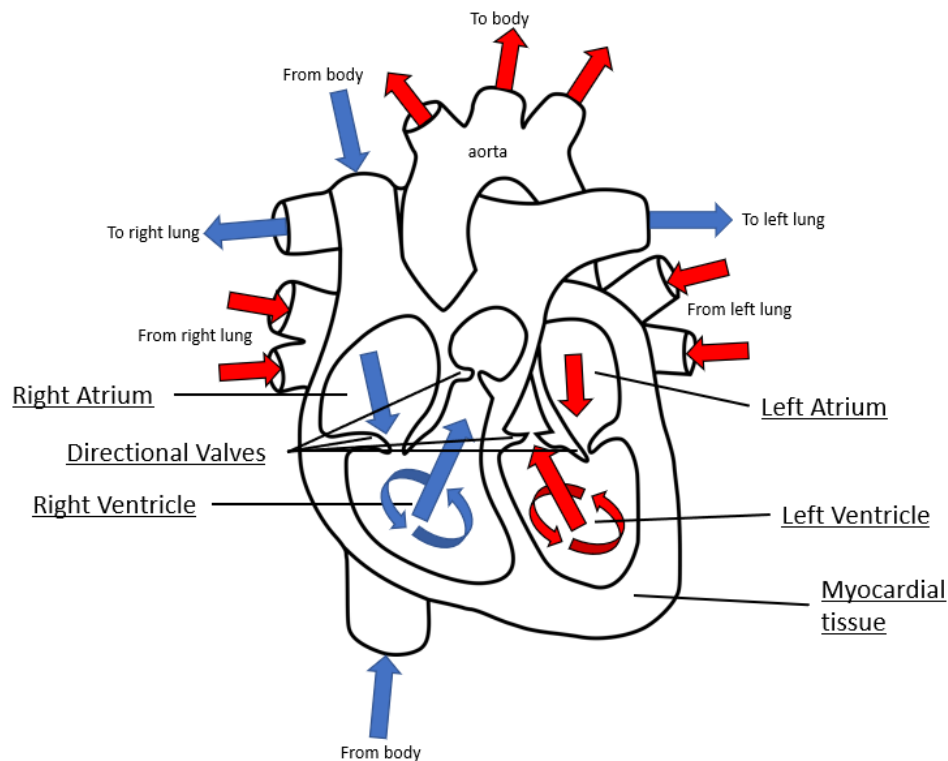
Figure 1-1 Heart Anatomy

1.1.2 « The Cardiac Cycle »

The cardiac cycle is broadly divided into diastole, and systole, when the left ventricle is either relaxed or actively contracting, respectively. Beginning near the end of diastole, the cardiac cycle starts by the electrical stimulation of the SA node which triggers the muscle in the atriums to contract; this is a gradient contraction as the signal travels through the muscle tissue and generates a "top-down" contraction pushing the blood from the atriums into the ventricles. This will increase the pressure in the ventricles and when atrial contraction is complete, the pressure in the ventricles will push the blood towards the atrium. At this time, the directional valves which only allow flow into the ventricles will close keeping the blood in the ventricle. The volume of blood in the ventricles, and specifically in the LV is called the end diastolic volume (EDV). Next, as signalled by the AV node, the ventricles and papillary muscles contract, starting systole. This contraction is called isovolumetric because the blood volume in the chamber does not change, however, the blood pressure increases rapidly. The role of the papillary

muscles in this stage is to keep the two valves leading to the atriums closed to prevent back flow. The role of the ventricle muscle is to increase the blood pressure itself.

Blood ejection occurs when the pressure in each of the respective ventricles overcomes the pulmonary and aortic valves previously kept shut by back pressure from the lung and aortic vasculature. The blood is then pushed out of the ventricles and into the respective veins and arteries. The difference in regions supplied by the blood just mentioned explains the geometric different in the right and left ventricles. While the RV only supplies blood to the lungs, the left ventricle must supply a pressure differential to ensure blood flow in the rest of the body requiring more muscle mass and generated pressure.

The ventricles are then triggered to relax via depolarization which is discussed in Section 1.1.3 and the ejection pressure begins to decrease starting diastole. Eventually, the pulmonary and aortic valves close once a relative backwards blood pressure is generated. At this point, all the valves in the ventricles are shut and the remaining volume is called the end systolic volume (ESV). In time, as the ventricles continue to relax, the atriums which have been passively filling this whole time will have enough pressure to push open their valves filling the ventricles with blood again waiting to be signalled to contract via the SA node once again, resetting the cycle.

1.1.3 « Myofiber Contraction Mechanism »

Cardiac muscle tissue is compromised of the cardiac muscle cells (myocytes) which contain the cardiac muscle fibers (myofibers) that generate contraction, and the extracellular matric (ECM) (Liang, 2019). More details on the general composition of cardiac tissue is discussed in Chapter 3.

Like skeletal muscle, myofiber contraction is governed by the activation of gated ion channels which cause contraction of the myofibers (Bers, 2002). Initially, the ion concentration in, and out of the cell is regulated by sodium potassium channels keeping sodium out of the cell, and potassium in. When an action potential caused by the sudden change in ion gradient reaches the myocyte via a gap junction, a voltage gated sodium

channel opens allowing positive sodium ions into the cell making the localized region positively charged. During this time, and due to the depolarization of the cell potential, a voltage gated calcium channel opens allowing calcium to enter the cell. The influx of calcium from the external cell environment then triggers the sarcoplasmic reticulum to release more calcium into the cell. This excess calcium in the cell released by the sarcoplasmic reticulum is responsible for the active contraction of the myofiber as described by the sliding filament model (Spudich, 2001).

1.2 « AMI and Diagnosis/Prognosis »

1.2.1 « Acute Myocardial Infarction »

Based on genetics and lifestyle, it is common for humans to experience varying degrees of atherosclerosis throughout their lifetime where fatty plaque is built up in the coronary arteries (Gomar, 2016). In extreme cases where a coronary artery becomes fully blocked by either plaque breaking off or a clot that blocks blood flow, the cardiac tissue downstream experiences ischemia. This event is called acute myocardial infarction. Until the blockage is removed, the tissue downstream will continue being damaged, leading to more and more cell death. To treat the ischemic event, revascularization is performed as soon as possible to minimize damage to the cardiac tissue and preserve the function of the heart (Allman, 2002).

In cases where AMI leads to tissue necrosis, that necrotic area suffers irreversible damage and transforms into infarct tissue with near zero contraction during the cardiac cycle (Canty,2012). This infarct tissue causes a series of problems which may ultimately lead to heart failure. It affects the electrophysiology of the heart, hence impacts the contraction timing which may require resynchronization therapy (Reumann, 2007; Kerckhoffs, 2008). It causes stress concentrations in the surrounding border zone, hence impacts signalling for mechanotransduction which may lead to cardiac remodelling (Hunter, 2012). Since the tissue contracts minimally or not at all, it also does not contribute to the required pressure build up ejecting blood during the cardiac cycle leading to a reduced efficiency. Lastly, during the first few days post myocardial infarction, the necrotic area is extremely weak and may rupture leading to immediate

death (Talman, 2016). Progress made pertaining to these issues using biomechanical models is discussed in Section 1.7 of this chapter.

In tissue regions where ischemia occurs without necrosis, the tissue is considered salvageable (Francone, 2009). In the salvageable area, some myocytes go into what is called a "stunned" or "hibernating" state based on whether the ischemic event is acute or chronic, respectively. In either state, while still viable, the cardiomyocytes function at a reduced metabolic rate where their contractile output is not as strong as healthy cells. This is, in part, is due to ischemic myofibers becoming "leaky" leading to an inability to maintain ion gradients required for contraction (Garcia-Dorado, 2012).

As a result, the mechanical output loss of the myocardium can range from only minor loss of contractility to full loss of contractility (Nakamura, 2015). To asses the damage to the myocardium quantitatively, the difficulty lies in determining whether the cardiomyocytes are dead or only stunned. More interesting is the possibility of quantifying this damage towards predicting future heart function and recovery. This introduces the concept of biomarkers which are used explicitly or implicitly to measure damage and provide information of future function of the heart.

1.2.2   « Biomarkers »

A biomarker is a quantitative measurement which acts as an indicator for normal or pathologic state, or pharmacologic response to therapeutic intervention. A biomarker must be accurate, precise, and have high sensitivity and specificity. It also beneficial if the biomarker is calibratable to patient specific requirements from epidemiology (Dhingra 2017, Gomar 2016). Biomarkers can be broken down into prognostic, pharmacodynamic, and predictive for CVD where prognostic indicates future disease progression, predictive indicates who is likely to benefit from treatment, while pharmacodynamic measures the effect of a drug. While a biomarker may generally relate to multiple different diseases or organ failure, it is desirable that a new biomarker provides information to aide in critical decision making. For instance, rating a patient risk beyond the standard clinical biomarkers (Dhingra 2017).

1.2.3 « Standard Biomarkers for diagnosing AMI »

Troponin I blood concentration remains the gold standard for AMI diagnosis (Chen, 2019). In AMI, the myocyte lysis caused by ischemia in the cardiac muscle tissue releases this protein into the blood stream. This increase in troponin I concentration can be measured to the requirements of a good biomarker and is the current gold standard (Keller 2009, Katus 1990).

1.2.4 « Novel Biomarkers for AMI »

Blood B-type natriuretic peptide (BNP) is the most exciting of novel biomarkers for AMI due to its classification as a prognostic biomarker which no other biomarker confidently offers. It is generated by myocytes when the ventricles undergo tension and has been able to predict heart failure post-AMI in-hospital and 180 days post infarct event (Chen, 2019). Unfortunately, the prognosis provided by this biomarker revolves around death, and the biomarker does not provide information on how the treatment may be possibly changed to minimize those odds.

There are a variety of other biomarkers currently under study, but they also suffer from lack of significant prognostic value or low sensitivity and specificity (Dhingra 2017, Chan 2010, Aydin, 2019, Chen 2019).

1.2.5 « Medical Imaging »

To aide in determining the extent of damage post AMI, medical imaging is a common tool used to image the heart and acquire more information on the state of the patient (Kinno, 2017). This information can be used to determine mechanical, geometric, and functional parameters.

Mechanical information on the state of the heart refers to how the heart deforms during contraction. This can be quantified simply as the ejection fraction (EF) of the heart which is shown in equation 1 below calculated using end systolic volume (ESV) and EDV.

$$EF = \frac{EDV - ESV}{EDV} \tag{1}$$

While ejection fraction is a good indicator of heart function in general, there is a large proportion of cases where patients suffer heart failure while ejection fraction is preserved (Hummel, 2017). Another general measure of the heart mechanical function is cardiac output. Cardiac output is the amount of blood pumped by the heart measured in litres per minute. While not limited to being measured with medical imaging, a low cardiac output is known to be related to heart failure (Vincent, 2008).

More in-depth mechanical information comes in the form of wall motion irregularities (Tee, 2013). Since the left ventricle is near symmetric along the short axis, areas that are damaged with reduced contraction force can be seen quite easily as areas that don't move as much in collected cardiac cine data. This is quantified via wall thickness at end diastole versus end systole, and even better as the strain (or displacement differential between the two states) as discussed in Section 1.4.1. of this thesis. Current medical imaging devices capable of capturing this information accurately are Ultrasound, dynamic contrast enhanced CT (DCE-CT), and MRI (Tee, 2013).

Geometric information is information regarding the extent of damage as seen with medical imaging. This primarily involves quantification of scar tissue and amount of salvageable tissue which is of interest as data supports the relationship between amount of scar tissue, and patient prognosis (So, 2017; Florian, 2011). This information can be acquired using DCE CT and MRI techniques.

Lastly, functional information is blood perfusion throughout the cardiac tissue. Perfusion can indicate regions that are still viable though damaged post AMI. This can be acquired using US, DCE-CT, MRI, and positron emission tomography (Ora, 2019).

All this measurable information is extremely valuable to the clinic with a lot of development in research dedicated to these imaging techniques. One general issue with data obtained from the mentioned imaging techniques, however, is that they only represent the state of the heart at the imaging time. While this is extremely valuable for triaging patients and diagnosing AMI, they cannot provide final prognostic information, for instance final scar volume, or predict the state of the patient's heart after revascularization without a second scan later on increasing overall cost.

A complement to medical imaging is biomechanical modelling. Modelling techniques offer new information only capable of being measured with the imaging modalities described above but have the potential for enhanced prognosis and predictive medicine. Advancements in the field of AMI cardiac modelling are described in Section 1.7.

1.3 « Theory: Continuum Mechanics »

Before discussing cardiac modelling, it is important to cover the fundamental concepts and mathematics that go into the formulation of continuum mechanics for cardiac modelling. Presented theory in this section is based on [Ogden, 1997; Holzapfel, 2010; Spencer, 2013].

1.3.1 « Stress and Strain »

To describe the deformation of the material, we need to have a fundamental understanding of stress and strain. When a force acts on a body, point loads cannot truly exist and act as loads over an area δA. Considering point P in Figure 1-2, we examine the "stresses" $\vec{t}$ caused by an external force acting on point P. We enclose a surface cube surrounding P in its own axes and write out an equation for each component of $\vec{t}$ as a summation of the components of $\vec{t}$ acting in the direction of each of the particles reference frame coordinates e_{ii} shown in equation 2.

$$\vec{t}_1 = t_{11}\vec{e}_1 + t_{12}\vec{e}_2 + t_{13}\vec{e}_3$$

$$\vec{t}_2 = t_{21}\vec{e}_1 + t_{22}\vec{e}_2 + t_{23}\vec{e}_3 \qquad (2)$$

$$\vec{t}_3 = t_{31}\vec{e}_1 + t_{32}\vec{e}_2 + t_{33}\vec{e}_3$$
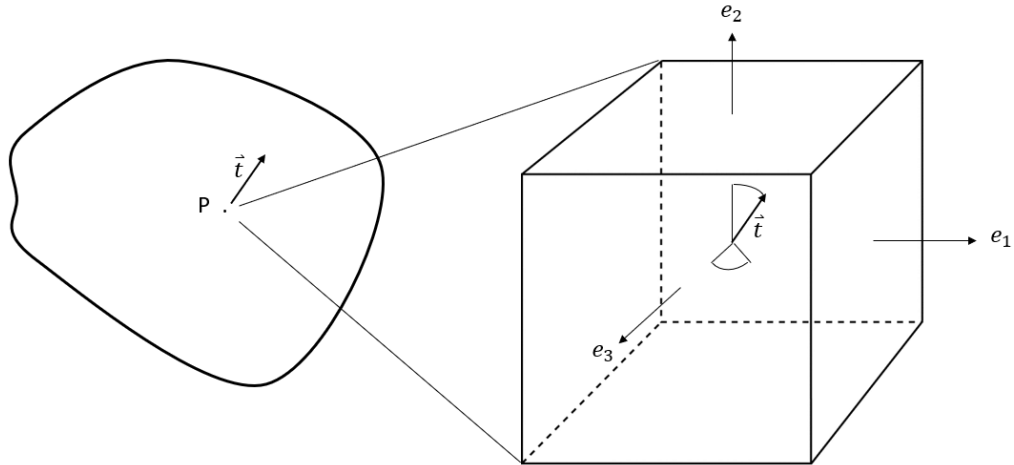
Figure 1-2 Point load acting on a point P enclosed by an ideal volume.

We can express this relationship compactly as follows:

$$\vec{t} = T_{ij}e_j \qquad (3)$$

Where T_{ij} is a second order tensor. Under the assumptions of Newton's 3rd law, it can be shown that $T_{ij} = T_{ji}$ and thus T_{ij} is a symmetric tensor. The values of T_{ij} are called stress components. For instance, T_{23} is the 2nd component of $\vec{t}$ in the direction of $\vec{e_2}$. This finding will be used later after a proper understanding of the strain is developed.

To develop an understanding of strain, object *deformation* is first described. An object deforms if it's shape changes during movement, i.e. body translation and rotation do not cause deformation.

Under deformation, a point X in the original volumes shape S moves to a new point in x shown in Figure 1-3.
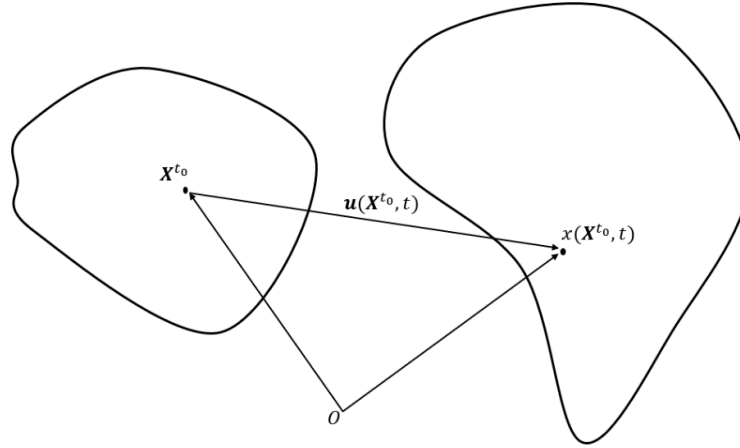
Figure 1-3 Particle displacement in time following a deformation.

The particle has moved by a displacement vector *u* which is a function of initial position and time. Given known values of X and x, we can solve for *u* using the following relationship:

$$u(X, t) = x(X, t) - X \tag{4}$$

For small deformation, differentiating the above equation can be performed by differential calculus as

$$\frac{\delta u(X,t)}{\delta X} \delta X = \frac{\delta x(X,t)}{\delta X} \delta X - \delta X \tag{5}$$

Rearranging the equation leads to:

$$\frac{\delta u(X,t)}{\delta X} = \frac{\delta x(X,t)}{\delta X} - \mathbf{I} \tag{6}$$

$$\frac{\delta x(X,t)}{\delta X} = \mathbf{I} + \frac{\delta u(X,t)}{\delta X} \equiv \mathbf{F} = \mathbf{I} + \nabla \mathbf{u} \tag{7}$$

where **I** is the identity matrix, $\nabla \mathbf{u}$ is the deformation gradient representing strain components, and **F** is the deformation gradient tensor.

It is noteworthy that while $\delta x = \mathbf{F} \delta X$, as mentioned above, the deformation must be independent of rotation and translation. Omitted here, it can be shown that δx is not equal

$\delta \boldsymbol{X}$ under rotation using this relationship. Taking the square of this relationship provides the equation below:

$$\delta x^2 = \delta \boldsymbol{X} \mathbf{F}^T \mathbf{F} \delta \boldsymbol{X} \tag{8}$$

which does not change under rotation. Hence, the second order tensor $\boldsymbol{C}$ is introduced which is equal to $\boldsymbol{F}^T \mathbf{F}$ and is called the *right Cauchy-Green deformation tensor*. It can be shown that $\boldsymbol{C}$ can be completely described by the displacement gradient $\nabla \mathbf{u}$ given in the equation below:

$$\mathbf{C} = \mathbf{I} + \nabla \mathbf{u} + \nabla \mathbf{u}^T + \nabla \mathbf{u}^T \nabla \mathbf{u} \tag{9}$$

This equation can be simplified by defining E as the *Green-Lagrange strain tensor* equal to one half of all terms involving the displacement gradient, leading to the equation:

$$\mathbf{C} = \mathbf{I} + 2\mathbf{E} \tag{10}$$

with

$$\mathbf{E} = \frac{1}{2}(\boldsymbol{C} - \boldsymbol{I}) \tag{11}$$

1.3.2 « Hyperelasticity »

Under small deformation, the tensor $\mathbf{C}$ can be simplified if we assume all higher orders of $\nabla \mathbf{u}$ are negligible leading to the field of linear elasticity. In the heart, it's uncommon for tissue to undergo small deformation, hence, any discussion on linear elasticity is omitted in this context while finite deformation which is associated with intrinsic change in mechanical properties causing nonlinear elasticity, or "hyperelasticity" is accounted for.

To relate stress to strain in the context of hyperelasticity, attention is drawn to strain energy which is the energy stored in the body undergoing deformation. When a body is subjected to a force it generates kinetic energy in the form of work acting on the body. In a conserved system, this energy must be equal and opposite to some other form of energy. For materials, this is considered an energy stored in the deformation of a material, for instance, when a piece of rubber is stretched and held under constant force,

the rubber deforms until equilibrium is reached. When it is let go, the stored deformation energy is released, and the rubber returns to its original shape. It is assumed that this energy is stored solely in the form of deformation, leading to the concept of *strain energy density* used as a measure of the material's strain energy. A function of this energy is called a *strain energy density function* typically denoted by W.

From a well-developed theory which is not discussed here, the following relationship between stress, strain in terms of W as a function of F is given.

$$T_{ij} = \frac{\rho}{\rho_0} F \frac{\partial W(F)}{\partial F} \tag{12}$$

Where the ρ's are the volume ratio of the material and can be computed as the determinate of **F**. If a material is incompressible, as often used in this thesis, the volume ratio is 1.

It is more common to express this equation in terms of the invariants of **C**. We start by defining stretch, as $\lambda_{ii} = 1 + \nabla u_{ii}$ or one plus the strain for each principal direction in the material coordinate system. From tensor properties, each tensor has a set of scalars that are invariant under choice of coordinate system. For C, defined in terms of stretches the invariants are

$$I_1 = \lambda_1{}^2 + \lambda_2{}^2 + \lambda_3{}^2$$

$$I_2 = \lambda_1{}^2\lambda_2{}^2 + \lambda_2{}^2\lambda_3{}^2 + \lambda_3{}^2\lambda_1{}^2 \tag{13}$$

$$I_3 = \lambda_1{}^2\lambda_2{}^2\lambda_3{}^2$$

W can now be expressed as a function of $I_1, I_2,$ and I_3. As such, for incompressible isotropic solids, the equation relating stresses to strains above is compactly written as

$$T_{ij} = -pI + 2W_1B - 2W_2B^{-1} \tag{14}$$

Where B is the left Cauchy green deformation tensor defined as $\mathbf{F}\mathbf{F}^T$ and W_i refers to the differentiation of W with respect to the numbered invariant.

1.3.2.1 « Different Forms of Strain Energy Density Equations »

Specific forms of W have been proposed to model different types of tissue and non-linear materials in general. These functions range from very simple, where a single material constant is involved, to increasingly complex with material constants numbering in the 10+ range. Used extensively in this thesis are 2 of these functions in their isotropic incompressible form. One is the Yeoh strain energy density function W which is given below:

$$W = \sum_{i=1}^{3} C_{i0}(I_1 - 3)^i + \frac{1}{D_i}(J - 1)^{2i} \qquad (15)$$

where J =1 with incompressible material and the second term vanishes, and the C's are the material's hyperelastic coefficients.

The second function used in this thesis is the Ogden strain energy density equation shown below. A major difference between this function and the Yeoh is that the value N representing the order of the function can in theory can lead to infinite sum, though in this thesis only 2nd and 5th order functions are used. In this function, the μ_i's and α_i's are the hyperelastic coefficients. Also, to note, is that this strain energy density function is based on the stretches, instead of the invariants discussed above.

$$W = \sum_{i=1}^{N} \frac{\mu_i}{\alpha_i}(\lambda_{jj}{}^{\alpha_i} - 3)^i \qquad (16)$$

1.3.3 « Finite Element Method »

The relationship between stress and strain established in the previous section and linked via strain energy density equations is required for the understanding of the storage of energy in deformation. In terms of solving continuum mechanics problems arising in the context of the heart mechanics where complex motion is involved, other tools are necessary for formulating effective computational solutions.

Conservation equations such as conservation of mass, momentum (linear and angular), and energy are all required to solve the continuum mechanics equations before tissue deformation and stress fields can be computed. In general, these equations are typically

partial differential equations with no analytical solution. To find approximate solutions, the finite element method (FEM) is employed where the solution domain is discretized into finite elements where the solution is sought at a set number of points called elements nodal points. This discretization leads to a system of equation which can be solved simultaneously to determine the solution of motion and stresses generated based on given loading. This method is employed in this thesis via ABAQUS, a commercial finite element solver (Dassault Systems Simulia Corp, USA).

1.3.4 « Hill's Model »

Cardiac muscle tissue can be considered active tissue due to its internal generation of forces which lead to the contraction and pumping of blood throughout the body. To properly model this action, the commonly used Hill's model formulation is applied in this thesis (Hill, 1938).

Hill's model has 3 components to model the whole tissue response of contracting tissue. The first two components are an "active" element, and a "passive" element connected in series as shown in Figure 1-4. The third component is another passive element connected in parallel with the other two elements in series. The combination of these elements represents a composite material tissue where in terms of the heart or muscle in general, the active component represents the possible contraction of the myofibers. As discussed above, when myofibers deform during contraction, internal stress is generated leading to contractile deformation. This deformation is resisted by myofibers themselves which are represented by the passive element connected in series. The passive element connected in parallel represent the surrounding extracellular matrix (ECM) of the myofibers that fill the empty space in cardiac tissue. Assuming the myofibers and ECM are fused such that there is "no-slip" when the myofiber contracts, the ECM must also deform with the myofibers and thus the resistance is the mechanical properties for the defined ECM.

The described Hill's model is known to have some limitations, including lack of viscoelastic response (Bovendeerd, 1996). While this is known to exist in the heart in-vivo, it is not currently modelled to avoid model complexity associated with challenging computational solution.

Active Element

Passive Element
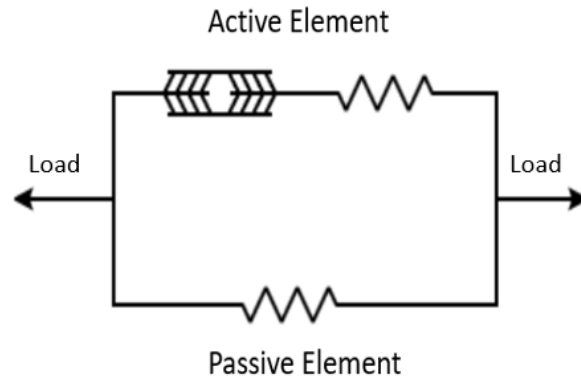
Figure 1-4 Hills Model

The implementation of Hill's model in ABAQUS is described in Chapter 2 of this thesis.

1.4 « Theory: Inverse Problems »

Presented theory in this section is based on [Chong, 1996; Reklaitis, 1983; Saad, 2003].

In the field of modelling, a model that takes an input and produces an output is called a forward model shown in equation 17 where x_i refers to a vector of input parameters to the model.

$$Output = F([x_1, x_2 \dots x_N]) \qquad N = [0, \infty) \qquad (17)$$

In many situations however, only the output is measured, and the inputs are what are sought after. In this situation, the inverse model of F is required to determine the inputs based on outputs.

$$[x_1, x_2 \dots x_N] = F^{-1}(Outputs) \qquad N = [0, \infty) \qquad (18)$$

In complex systems such as in finite element modelling, the inverse forward model does not exist and must be solved through optimization.

1.4.1 « Mathematical Optimization »

Mathematical optimization is a solution often adapted to solve inverse problems. It can be used to maximize or minimize a function of choice which, in this case, will be called the

"cost" function. Note, the maximum of a function is just the minimum of the negative form of the function, and from here onward, only the term minimization will be used.

To solve the inverse problem above for the unknown inputs, optimization is the process of changing inputs to the forward model to best match the measured outputs. If the outputs are known, and inputs of a forward model generate different outputs, the different between the two outputs at discretized points are called the error. The cost function of most optimization techniques is to minimize this error shown in Equation 19.

$$[Error_i] = MeasuredOutputs_i - F([x_1, x_2 \ldots x_N]) \quad N = [0, \infty), j = [1, \infty) \quad (19)$$

1.4.2   « Nonlinear Least Squared Optimization »

When a function is nonlinear, iterative optimization is required were the inputs to the forward model are put in as an initial guess, and then changed until the minimum cost function is reached. In the case of least squares optimization, the cost function is modified from above to be the equation below, where the error is now minimized with reference to magnitude of the sum of squared differences between measured and computed outputs.

$$[Error_i] = \|MeasuredOutputs_i - F([x_1, x_2 \ldots x_N])^2\| \quad N = [0, \infty), i = [1, \infty) \quad (20)$$

During this iterative process, initial guess parameters starting the optimization are changed by a step size in the direction of a lower cost function until convergence is achieved.

There are many techniques to reach the minimum cost function using 1st and higher derivates of the cost function to compute the step size and direction. Commonly, second degree quadratic information is used which compute the first derivative (or gradient), and the second derivative (or Hessian) of the function. With this information, different techniques can be used to determine the minimum cost and optimal input parameters. In this thesis, MATLAB's r2019a developed trust region reflective optimization methodology is used.

Least squares solutions using gradient methods work very well for functions that are known as seen in Chapter 4. When treating unknown or extremely complex functions with potentially many local minima, they can suffer from converging to a local minimum instead of the global minimum which often represent the sought solution. Techniques to minimize the possibility of convergence to local minima include using constrained optimization where the parameters are given lower and upper bounds to their possible value, though the true local minimum is still not guaranteed.

1.4.3 « Genetic Algorithms »

Genetic algorithms (GA) are one of many types of optimization techniques to overcome convergence to local minima. They do not follow gradient based optimization, but rather stochastic processes which take the cost function into account as "fitness" of an individual (Fraser, 1970).

Genetic algorithms start with an initial guess input by the user to start the technique. From the initial guess, a "population" of "individuals" is stochastically generated by perturbations to the initial guess as shown below where the λ's are perturbations to the initial guess within constraints given by the user.

$$Initial guess = [x_1, x_2 \dots x_N]$$

$$Population_1 = \begin{bmatrix} [x_1, x_2 \dots x_N] \\ \vdots \\ [\lambda_{i1}x_1, \lambda_{i2}x_2 \dots \lambda_{iN}x_N] \end{bmatrix} \qquad (21)$$

$$Where\ N = [0, \infty), \ \ i = [1, MaxPopulation)$$

The "diversity" refers to how different the λ's will be and is set before optimization. Each individual in the population is run through the forward model and all fitness's are calculated.

The individuals with the best fitness are called "elites" who immediately become an individual in the next population. The remaining individuals with the best fitness from the first population are selected and become "parents" of the next generation. From the

selection of elites and parents a new population is generated through events called "mutations" and "crossovers". A mutation is a random permutation to one of the parent values, and a crossover is the blended values of two random parents. Based on the pre-set numbers of elites, and percentages of mutations and crossovers, the new "generation" of the population is generated. The process of generating a new population is shown in Figure 1-5.

$$Population_2 = \begin{bmatrix} Elites \\ Mutations \\ Crossovers \end{bmatrix}$$

Elite

$$Elite_i = [x_{i1}, x_{i2} \dots x_{iN}]$$

- -

Mutation

$$Parent_i = [x_{i1}, x_{i2} \dots x_{iN}]$$
$$mParent = [x_{i1}, \mu_* x_{i2} \dots x_{iN}]$$

- -

Crossover

$$Parent_i = [x_{i1}, x_{i2} \dots x_{iN}]$$
$$Parent_j = [x_{j1}, \dots x_{jN}]$$
$$cParent = [x_{i1}, x_{j2} \dots x_{iN}]$$
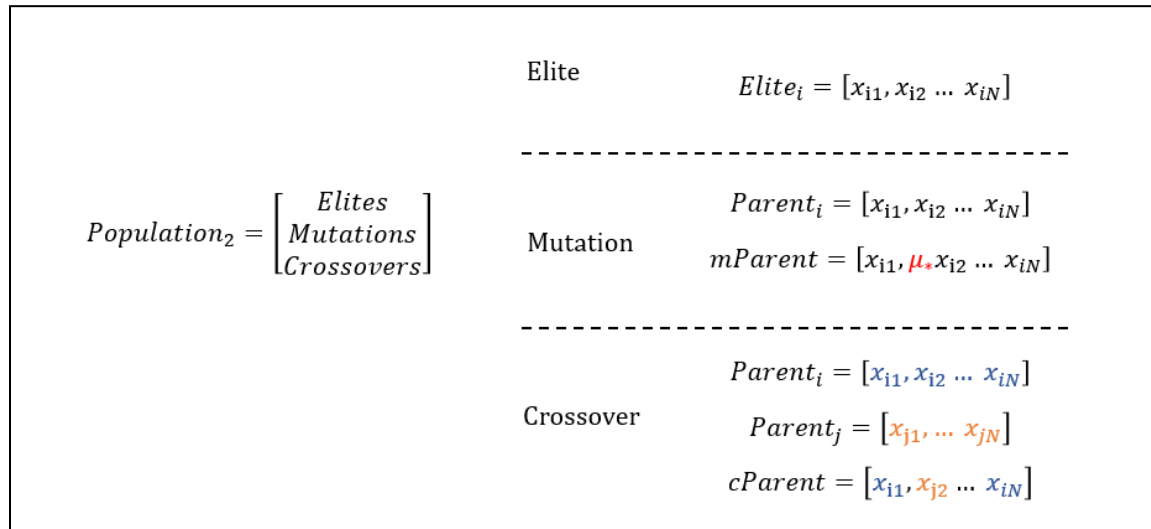
Figure 1-5 Possible events to generate a new genetic algorithm population.

After the new population is generated, the new individual fitness's are evaluated, and the cycle continues until convergence is achieved at the global minimum. Convergence in this technique can be deemed by a pre-set fitness level or any 1 individual, average fitness level multiple individuals, generation number, and other time constraints.

1.5 « Reduced Models »

In the context of estimating a biomechanical model's parameters using optimization, a forward model which computes the deformation of tissue for instance must be used to compute the cost function in each iteration. Forward models in this context are computationally expensive as their associated run times can be several minutes. As such, with iterative optimization techniques, it is common for times before convergence to reach a week, or in the case of genetic algorithms, months. To remedy this problem,

techniques to reduce complex forward models for faster run times are of high value (Mousavi, 2012). Among available techniques developed for this purpose, the technique described in the following section is considered to generate a reduced forward model in this thesis which involves statistical shape modelling and neural networks.

1.5.1.1 « Statistical Shape Modelling »

In the case of a LV FE where parameters are assigned to characterize contraction forces in various regions of the LV, several LV contracted shapes can be produced to sample the contracted shape space. If the output of the LV shape is of interest (see Chapter 2), the variability of these shapes can be expressed using a reduced model without significant loss or accuracy (Cootes, 1995). For this purpose, let's assume that there are N shapes being considered for this reduction where the purpose is capturing each of these shapes using only a small number of parameters. We assume that each shape is defined by a set of landmarks on the surface which represent the same location on all N shapes. In the context of LV shape modelling, if the FE mesh of each LV is generated following a single meshing scheme, this assumption is appropriate since each node (which is numbered consistently) will act as a landmark.

Each shape occupies a M*n-dimensional space where M is dimensions in original data (3 in the case of 3D) and n is the number of landmarks. N shape sets then occupy N points in this 3n-D space. To reduce the amount of variables to describe the shape, this new point cloud in 3n-D space can then be greatly reduced using principal component analysis, which finds a new, orthogonal set of axes within this 3n-D space which is structured such that each new axes reflects the most variance in the data in descending order.

To do this reduction, the covariance matrix of the sample set is first computed. This can be done by computing the covariance equation below for each element in the covariance matrix.

$$Cov(j,k) = \left(\frac{N}{N-1}\right) * \sum_{i=1}^{N}(x_j(i) - \overline{x_j})(k(i) - \overline{x_k}) \qquad (22)$$

In equation 22, j and k refer to the 3n-D×3n-D covariance matrix rows and columns respectively, $\overline{x_j}$ and $\overline{x_k}$ are the means of each variable for that dimension, and $x_j(i)$ referring to each of the separate data sets.

Complete, the covariance matrix can be expressed as C. From here, the eigenvalues (λ's) can be solved by equation 23

$$0 = det(C - \lambda I) \qquad (\ 23\ )$$

Where "det" is the matrix determinant of the interior bracketed covariance matrix and I is the identity matrix. From there each eigenvector can be calculated.

The benefit at this point is that unlike the previous orthogonal 3n-D space, we've generated a new 3n-D space which is also orthogonal, but the orthogonal dimensions are based on **C** where each dimension is now uncorrelated from the next. From here, the proportion of variance can be calculated by the eigenvalues and ranked from largest to smallest. In this order, we call the set of eigenvectors the principal components. A threshold for total percentage of the variance captured can be chosen, and the main principal components can be extracted to describe the data set.

After an appropriate number of principal components k is selected, the matrix **D** of the eigenvectors with size 3n-D×k is created. This is used to recast the original data into this new, dimension reduced form going from N data sets in 3n-D dimensions to N sets in k dimensions (Olver, 2018).

In summary, this allows the shape space to be described by several main modes that reflect the most important shape changes regarding shape variability. This allows any shape to be generated by a linear combination of these principal components which can then predict new, statistically likely shapes to come out of simulation.

1.5.1.2   « Neural Networks »

Neural networks are another approach to decrease the computation time of forward models. They provide a bridge between the forward model inputs and outputs without

using the forward model itself, but rather, is trained by the forward model to predict expected outcomes given inputs.

A neural network is a function of "layers" and "neurons" which connect input data to output data as shown in Figure 1-6. Each input is connected to each neuron in the first layer. The inputs are multiplied by a weight factor and the sum of all weighted inputs are then converted to a new value via a transfer function. The values of each neuron are then all connected to the neurons of the next layer with another set of weights, and the values propagate so forth until the final layer were the new outputs are computed. To determine the weights of the neural network, known data with inputs and outputs are used as a training set, and the weights are optimized using optimization techniques such that the neural network can accurately predict validation data using a separate set of test cases.

Once trained, the neural network can then predict new outputs based on given inputs replacing the computation of the forward model with little loss to accuracy provided the training set is adequately sampled within the function space.

The combination of the statistical shape model concept and neural networks has been used in this thesis to obtain reduced models of the LV FE. To this end, both LV geometry (input) and their contraction displacement fields (output) are considered shapes where PCA was used to express them using a small number of parameters. It is this version of compact input and output sets that are used to train the neural networks to produce reduced forward models. It is noteworthy that using the first step of PCA is critical as it leads to relatively straight forward neural network topology where overfitting and convergence are less likely (Mousavi, 2012).
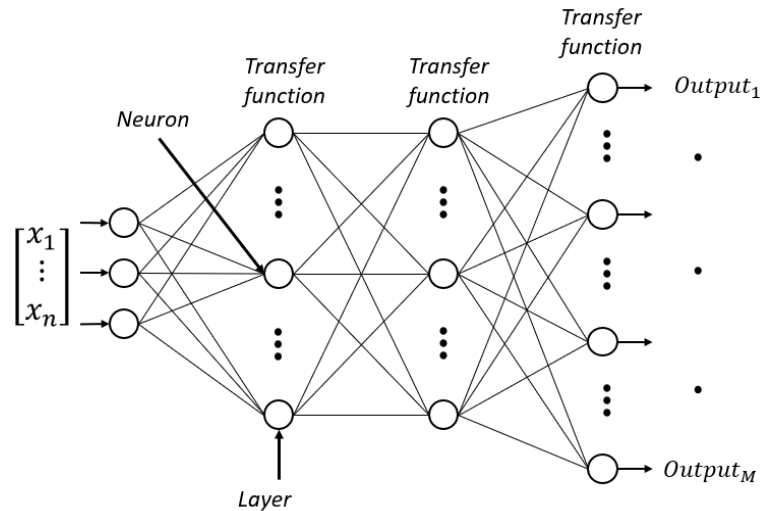
Figure 1-6 Example neural network topology

1.6 « Cardiac Modelling »

Cardiac modelling based on continuum mechanics described above combined with inverse problem formulation has emerged as an increasingly popular research area serving as a complementary technique applied to medical imaging. It provides information on the heart which is not possible to measure in the clinic. This information may be the key to better patient treatment who suffer from CVD's. While much CVD information is enhanced with cardiac modelling, we focus on its uses for patients who have suffered AMI.

The new information that biomechanical modelling can offer is cardiac stress, strain, contraction force, and mechanical properties or stiffness (Lopez-Perez, 2015). All these measurements may have a vital value in the clinic.

In-vivo cardiac stress is hypothesized as the main influencer for cardiac remodelling post AMI (Talman, 2016). This remodelling happens over years post MI and ultimately leads to heart failure. The mechanism for remodelling is mechanotransduction where stresses are felt by the cells and remodelling is triggered to lower these stresses (Yang, 2002). There are only few studies to date dedicated to investigating this as the predictive problem in this case is quite complex. However, there is some literature that suggests the optimization of cardiac mechanical properties and geometry ultimately serves to reduce

this stress (Yamazaki, 1999; Weber, 2013). It is anticipated that cardiac modelling will greatly enhance this field being the only technique capable to estimate these values.

While strains can be measured using medical imaging alone, they are typically aligned within conventional axes defined by the AHA model which is short, long, and horizontal axis (Aletras, 2006). Strain values measured from these directions do not represent the true principal strain of the tissue where no shear strain exists. A recent study showed the capability of cardiac modelling to measure the principal strain from medical imaging which may be a better marker of infarct scar region than conventional image enhancement techniques (Satriano, 2017).

Cardiac contraction forces and mechanical properties are the main attraction of cardiac modelling and the literature is extensive (see Chapters 2 and 3 respectively). These are tuneable parameters in cardiac models which really show the strength of this field by measuring the mechanical output of the myocytes as well as providing knowledge on the regional variability of tissue structure. To predict these parameters, a model based on the geometry of the heart is generated and the mechanical properties and contraction forces can be optimized within an inverse problem framework described in Section 1.4 (though potentially with different optimization techniques) to predict the patient specific values. Once predicted, these parameters can be changed to simulate new function of the heart once healed.

To date, the closest application of cardiac modelling in the clinic is related to resynchronization therapy (Krozier, 2016, Willeman, 2019). No clinical use has been presented to date for contraction force and mechanical properties estimation due to the high cost of follow up data required to validate the techniques presented in the literature, or perceived lack of clinical value.

1.7 « Objectives »

The primary objective of this thesis is to generate new predictive and prognostic biomarkers based on their contraction derivable from cardiac imaging and modelling for

hearts that have suffered myocardial infarction to enhance the clinical use of cardiac modelling.

Chapter 2 of this thesis presents a new technique to predict healthy and stunned myofiber contraction forces. This technique differs from those presently in literature as this technique does not require tissue tracking methods but rather, uses just the shape geometry within an inverse optimization framework. This significantly reduces the cost of imaging applied in techniques referenced in Chapter 2 while it also allows CT to be used in cardiac modelling which has never been done. Techniques presented in this chapter also introduce novel contraction variables which can predict future necrotic tissue along with myofiber healing. To the best of my knowledge, no cardiac model has been introduced for the latter purpose. This model feature enables prediction a range of final infarct volume which has high prognostic value. It also allows for prediction of healed ejection fraction and cardiac output which are currently used to evaluate the state of the heart in the clinic.

Chapter 3 offers a promising and easily implementable technique to accurately model the mechanical properties of scar tissue and stage its healing. This is based on a micro-to-macro FE model of cardiac tissue which is reduced using neural networks to predict how well the patient infarct heals relative to population values. This technique has the benefit of predicting the microconstituent tissue composition which may indicate risk of left ventricle rupture for which there is treatment available.

Chapter 4 presents a study aimed at a future investigation to validate the expected range of performance coming from Chapter 2. In the clinic, there remains a decision of when to trigger medical imaging collection during the cardiac cycle. Though chapter 2 requires both end systole and end diastole, validation metrics to evaluate the model can be generated from either image set. Specifically, a validation metric relating to the general function of the beating heart is cardiac output measured by indicator dilution techniques. We investigated the effect of what time during the cardiac cycle is more accurate for our interest. Chapter 5 closes the thesis by concluding our findings and presents the future work of this area of study.

« References »

1. Aletras A. H., et al, "Retrospective determination of the area at risk for reperfused acute myocardial mnfarction with T2- weighted cardiac magnetic resonance imaging," American Heart Association, 113, 1865-1870 (2006).

2. Allman, K. C., Shaw, L. J., Hachamovitch, R., & Udelson, J. E. (2002). Myocardial viability testing and impact of revascularization on prognosis in patients with coronary artery disease and left ventricular dysfunction: A meta-analysis. *Journal of the American College of Cardiology*, *39*(7), 1151–1158.

3. Asner, L., Hadjicharalambous, M., Chabiniok, R., Peressutti, D., Sammut, E., Wong, J., … Nordsletten, D. (2017). Patient-specific modeling for left ventricular mechanics using data-driven boundary energies. *Computer Methods in Applied Mechanics and Engineering*, *314*, 269–295.

4. Aydin, S., Ugur, K., Aydin, S., Sahin, İ., & Yardim, M. (2019). Biomarkers in acute myocardial infarction: Current perspectives. *Vascular Health and Risk Management*, *15*, 1–10.

5. Benjamin, E. J., Virani, S. S., Callaway, C. W., Chamberlain, A. M., Chang, A. R., Cheng, S., … Muntner, P. (2018). Heart disease and stroke statistics - 2018 update: A report from the American Heart Association. In *Circulation* (Vol. 137).

6. Bers, D. M. (2002). Cardiac excitation–contraction coupling. *Nature*, *415*(January), 13–17.

7. Bovendeerd, P. H. M. (2012). Modeling of cardiac growth and remodeling of myofiber orientation. *Journal of Biomechanics*, *45*(5), 872–881.

8. Bovendeerd, P. H., Arts, T., Delhaas, T., Huyghe, J. M., van Campen, D. H., & Reneman, R. S. (1996). Regional wall mechanics in the ischemic left ventricle: numerical modeling and dog experiments. *American Journal of Physiology-Heart and Circulatory Physiology*, *270*(1), H398–H410.

9. Canty, J. M., & Suzuki, G. (2012). Myocardial perfusion and contraction in acute ischemia and chronic ischemic heart disease. *Journal of Molecular and Cellular Cardiology*, *52*(4), 822–831. https://doi.org/10.1016/j.yjmcc.2011.08.019

10. Chan, D., & Ng, L. L. (2010). Biomarkers in acute myocardial infarction. *BMC Medicine*, *8*.

11. Chen, Y., Tao, Y., Zhang, L., Xu, W., & Zhou, X. (2019). Diagnostic and prognostic value of biomarkers in acute myocardial infarction. *Postgraduate Medical Journal*, *95*(1122), 210–216.

12. Cootes TF, Taylor CJ, Cooper DH, Graham J. 1995. Active shape models – their training and application. Comput Vis Image Understand. 61(1):38–59.

13. Crozier, A., Blazevic, B., Lamata, P., Plank, G., Ginks, M., Duckett, S., … Smith, N. P. (2016). Analysis of lead placement optimization metrics in cardiac resynchronization therapy with computational modelling. *Europace : European Pacing, Arrhythmias, and Cardiac Electrophysiology : Journal of the Working Groups on Cardiac Pacing, Arrhythmias, and Cardiac Cellular Electrophysiology of the European Society of Cardiology*, *18*, iv113–iv120.

14. Dhingra, R., & Vasan, R. S. (2017). Biomarkers in Cardiovascular Disease. *Trends in Cardiovascular Medicine*, *27*(2).

15. E.K.P. Chong and S.H. Zak, An Introduction to Optimization, John Wiley & Sons, Inc., New York, 1996.

16. Florian, A., Jurcut, R., Ginghina, C., & Bogaert, J. (2011). Cardiac magnetic resonance imaging in ischemic heart disease: a clinical review. *Journal of Medicine and Life*, *4*(4), 330–345.

17. Francone, M., Bucciarelli-Ducci, C., Carbone, I., Canali, E., Scardala, R., Calabrese, F. A., … Agati, L. (2009). Impact of Primary Coronary Angioplasty Delay on Myocardial Salvage, Infarct Size, and Microvascular Damage in Patients With ST-Segment Elevation Myocardial Infarction. Insight From Cardiovascular Magnetic Resonance. *Journal of the American College of Cardiology*, *54*(23), 2145–2153.

18. Fraser, Alex; Burnell, Donald (1970). Computer Models in Genetics. New York: McGraw-Hill. ISBN 978-0-07-021904-5.

19. G.V. Reklaitis, A. Ravindran, K.M. Gagsdell, Engineering Optimization: Methods and Applications, John Wiley and Sons, 1983.

20. Garcia-Dorado D, Andres-Villarreal M, Ruiz-Meana M, Inserte J, Barba I. Myocardial edema: a translational view. J Mol Cell Cardiol 2012;52:931-9.

21. Gray H., Standring S, Ellis, H, and Berkovitz, B. K. B., [Gray's Anatomy: The Anatomical Basis of Clinical Practice], Edinburgh: Elsevier Churchill Livingstone, 2005.

22. Hill, A. V. (1938). The heat of shortening and the dynamic constants of muscle. *Royal Society*, *126*(843), 136–195.

23. Holzapfel, G. A., [Nonlinear Solid Mechanics], Hoboken, John Wiley and Sons Inc., 2010.

24. Katus, H. A. (1991). Diagnostic efficiency of troponin T measurements in acute myocardial infarction. *Circulation*, *83*(3), 902–912.

25. Keller, T., Zeller, T., Peetz, D., Tzikas, S., Roth, A., Czyz, E., … Blankenberg, S. (2009). Sensitive troponin I assay in early diagnosis of acute myocardial infarction. *New England Journal of Medicine*, *361*(9), 868–877.

26. Kerckhoffs R. C P, Lumens J., Vernooy K., et al. Cardiac resynchro- nization: insight from experimental and computational models. Prog Biophys Mol Biol. 2008;97:543– 561.

27. Kinno, M., Nagpal, P., Horgan, S., & Waller, A. H. (2017). Comparison of Echocardiography, Cardiac Magnetic Resonance, and Computed Tomographic Imaging for the Evaluation of Left Ventricular Myocardial Function: Part 1 (Global Assessment). *Current Cardiology Reports*, *19*(1).

28. Liang, Z., San, T. R., Yin-kwee, N. E., [Computational and Mathematical Methods in Cardiovascular Physiology], World Scientific Publishing, 2019.

29. Lopez-Perez, A., Sebastian, R., & Ferrero, J. M. (2015). Three-dimensional cardiac computational modelling: Methods, features and applications. *BioMedical Engineering Online*, *14*(1), 1–31.

30. Mousavi, S. R., Khalaji, I., Naini, A. S., Raahemifar, K., & Samani, A. (2012). Statistical finite element method for real-time tissue mechanics analysis. *Computer Methods in Biomechanics and Biomedical Engineering*, *15*(6), 595–608.

31. Nakamura, M., Kido, T., Kido, T., Tanabe, Y., Matsuda, T., Nishiyama, Y., … Mochizuki, T. (2015). Quantitative circumferential strain analysis using adenosine triphosphate-stress/rest 3-T tagged magnetic resonance to evaluate regional

contractile dysfunction in ischemic heart disease. *European Journal of Radiology*, *84*(8), 1493–1501.

32. Ogden, R.W., [Non-linear elastic deformations], New York, Dover Publications, 1997.

33. Olver, P. J., Shakiban, C., [Applied Linear Algebra], Springer, 2018.

34. Ora, M., & Gambhir, S. (2019). Myocardial Perfusion Imaging: A Brief Review of Nuclear and Nonnuclear Techniques and Comparative Evaluation of Recent Advances. *Indian Journal of Nuclear Medicine |*, *34*(4), 359–362.

35. Reumann Matthias, Farina Dima, Miri Raz, Lurz Stephan, Osswald Brigitte, Dssel Olaf. Computer model for the optimization of AV and VV delay in cardiac resynchronization therapy. Med Biol Eng Comput. 2007;45:845-854.

36. Saad, Y., [Iterative Methods for Sparse Linear Systems], Society for Industrial and Applied Mathematics; 2nd Revised edition edition, (2003)

37. Sanchis-Gomar, F., Perez-Quilis, C., Leischik, R., & Lucia, A. (2016). Epidemiology of coronary heart disease and acute coronary syndrome. *Annals of Translational Medicine*, *4*(13), 256–256.

38. Satriano, A., Heydari, B., Narous, M., Exner, D. V., Mikami, Y., Attwood, M. M., … White, J. A. (2017). Clinical feasibility and validation of 3D principal strain analysis from cine MRI: comparison to 2D strain by MRI and 3D speckle tracking echocardiography. *International Journal of Cardiovascular Imaging*, *33*(12), 1979–1992.

39. So, A., Wisenberg, G., Teefy, P., Yadegari, A., Bagur, R., Hadway, J., … Lee, T. Y. (2018). Functional CT assessment of extravascular contrast distribution volume and myocardial perfusion in acute myocardial infarction. *International Journal of Cardiology*, *266*, 15–23.

40. Spencer, A. J. M., [Continuum Mechanics], dover Publications, 2013.

41. Spudich, J. A. (2001). The myosin swinging cross-bridge model. *Nature Reviews Molecular Cell Biology*, *2*(5), 387–392.

42. Talman, V., & Ruskoaho, H. (2016). Cardiac fibrosis in myocardial infarction—from repair and remodeling to regeneration. *Cell and Tissue Research*, *365*(3), 563–581.

43. Tee, M., Noble, J. A., & Bluemke, D. A. (2013). Imaging techniques for cardiac strain and deformation: Comparison of echocardiography, cardiac magnetic resonance and cardiac computed tomography. *Expert Review of Cardiovascular Therapy*, *11*(2), 221–231.

44. Vincent, J. L. (2008). Understanding cardiac output. *Critical Care*, *12*(4), 12–14.

45. Weber, K. T., Sun, Y., Bhattacharya, S. K., Ahokas, R. A., & Gerling, I. C. (2013). Myofibroblast-mediated mechanisms of pathological remodelling of the heart. *Nature Reviews Cardiology*, *10*(1), 15–26.

46. Willemen, E., Schreurs, R., Huntjens, P. R., Strik, M., Plank, G., Vigmond, E., … Lumens, J. (2019). The left and right ventricles respond differently to variation of pacing delays in cardiac resynchronization therapy: A combined experimental-computational approach. *Frontiers in Physiology*, *10*(FEB), 1–13.

47. Y.M., H., L.C.Y., L., C.S.P., L., D.F., F.-M., K., D., M., R., … E.S., H. (2017). Echocardiographic estimation of left ventricular and pulmonary pressures in patients with heart failure and preserved ejection fraction: a study utilizing simultaneous echocardiography and invasive measurements. *European Journal of Heart Failure*, *19*(12), 1651–1660.

48. Yamazaki, T., & Yazaki, Y. (1999). Role of tissue angiotensin II in myocardial remodelling induced by mechanical stress. *Journal of Human Hypertension*, *13*, S43–S47.

Chapter 2

2 « Characterizing Regional Myofiber Damage Post-Acute Myocardial Infarction Using Shape Optimization »

2.1 « Introduction »

Cardiovascular diseases (CVD) are the leading cause of death worldwide, contributing to ~31% of deaths worldwide in 2016 (W.H.O., 2017). Of the many cardiovascular diseases, coronary heart disease (CHD) is the deadliest, accounting for 44% of all CVD related deaths (Benjamin et al., 2018). In extreme cases, this disease can lead to acute myocardial infarction (AMI). In the time between the initial onset of AMI and revascularization of the coronary artery, the cardiac tissue downstream of the occlusion experiences ischemia. While the effect of ischemia varies based on the amount of peripheral blood flow provided by the collateral vasculature to the cardiac tissue, the result of any ischemia is damaged cardiomyocytes leading to depressed contractility (Camici, Prasad, & Rimoldi, 2008). This damage can be extreme where it can cause the cardiomyocytes to become necrotic leading to infarction whereas in other instances, the myocytes reduce their metabolic activity to avoid cell death (Kelly et al., 2011). This phenomenon of reduction in metabolic rate and depressed contractility is known as myocardial hibernation, or myocardial stunning when the ischemia is chronic or acute, respectively. While stunned myocardium can recover within weeks, hibernation can cause prolonged contractile damage over 3 months or can even potentially lead to permanent damage (Pasque, 2017). Devising effective treatment for each of these scenarios requires their reliable determination.

Several imaging methods exist to visualize the extent of ischemic and infarcted tissue. They include single-photon emission computed tomography, myocardial perfusion imaging using CT, or T1/ T2 weighted cardiac MRI to view ischemic regions. There is also late iodine enhanced imaging using CT, or late gadolinium enhanced imaging using MRI that are used to visualize infarct tissue (So et al., 2018; Kim et al., 2000; Wright et al., 2009). These imaging techniques show the location and size of the damaged region, providing valuable diagnostic information. Focusing on the ischemic imaging where the

myocytes are still viable, contrast for both the CT and MRI methods is typically via edema caused by necrosis and ischemia, or perfusion (So et al., 2018; Kim et al., 2000; Wright et al., 2009). A disadvantage of both contrasts is the stability of the area at risk. Edema is not stable and may lead to inaccurate morphological data of the ischemic tissue depending on when the imaging took place (Fernández-Jiménez et al., 2015), and perfusion images may vary based on inter- and intraobserver error (Larghat et al., 2013). Moreover, if imaging was conducted in a follow up session where the edema no longer exists, or the artery is reperfused, but the depressed contractile response persists, these imaging techniques alone would not suffice to determine the magnitude of remaining damage (e.g. contractile dysfunction) to the myocytes.

Another option to asses the heart function due to ischemia is through the analysis of dynamic motion of the myocardium during contraction. A common measurement for this motion is strain measurements, where the change in tissue local length can indirectly indicate ischemia with some accuracy (Norum, I. B. et al., 2015). Looking deeper, since the contraction of the heart is caused by myocytes, and by extension, myofibers, determining myofiber contraction characteristics of the damaged tissue could provide more direct diagnostic and prognostic information. While being patient specific, similar to what is provided through the previously described imaging techniques, this information can provide clinicians invaluable clues pertaining to expected functional recovery.

A technique that has the potential to measure many cardiac parameters effectively is founded on biomechanical modelling. It is a tool used to understand complex motion, deformation and internal force characteristics of different parts of the body. While being an effective predictor of tissue deformation, it can provide insight into the pathophysiological changes of organs and tissues as abnormal deformation can be a manifestation of such changes. Cardiac biomechanical modelling has been used to study the heart for over a century and has led to insights on tissue contractility (Chabiniok et al., 2012; Genet at al., 2015; Asner et al., 2016; Balaban et al., 2017; Finsberg at al., 2018), mechanical properties and changes during ischemia (Balaban et al., 2018; Haddad & Samani, 2017b; Nikou et al., 2016; Hadjicharalambous et al., 2017), as well as

knowledge on the complex fluid mechanics and the electrophysiology of the heart (Karabelas at al., 2018).

Common amongst all the current proposed techniques is the need to track the motion of the myocardium during its contraction. This allows the model to solve for the cardiac properties via inverse problem frameworks to best match the measured motion. This tracking is possible using MR tagging (Zerhouni et al. 1988, Radiology), MR phase imaging (Nayak et al., 2015), and speckle tracking echocardiography (Mor-Avi et al., 2011). MR tagging suffers from pattern fading, long acquisition time and low resolution. MR phase imaging has been used mainly for hemodynamics characterisation and is not commonly used in the clinic. Lastly, speckle tracking offers only low-quality motion information data. In this article, we propose a technique which can use conventional imaging modalities such as 3D ultrasound, MRI or CT in conjunction with biomechanical modelling to predict the myofiber damage post AMI in a left ventricle without the tissue tracking necessity. This is proposed via an inverse problem framework which does not require tissue motion data; it rather uses the shape of the LV pre- and post- contraction as input to output parameters characterising the myofiber damage. In this context, shape optimization involves automatically delineating the shape of the LV which is a straightforward procedure that can be performed using automatic image segmentation software. This technique can also be effectively used in conjunction with clinically used CT imaging, hence has the potential to be used as an effective clinical tool. It is noteworthy that unlike US and MRI that can be used for myocardial motion tracking, CT can be only used for myocardial shape characterization due to its low contrast. Our hypothesis is that finding optimal cardiac myofiber contraction forces that lead to the best shape matching between our computational biomechanical model and the segmented shape will give an accurate description of the ischemic damage. We investigate below a first test of this technique using in-silico generated LV biomechanical models.

2.2 « Methodology »

2.2.1 « Myocardial Contraction Force Reconstruction - Overview »

The proposed method takes surface shape data of the LV at two states of contraction as input. These states are mid diastole and end systole that represent the initialization state when the LV is relaxed, and the maximum contraction state, respectively (Genet at al., 2015). The surface shape data can be delineated by segmenting 3D cardiac image data captured at the two contraction states. Using this input, we have developed an algorithm used to reconstruct the LV contraction forces. Since the shape of the LV measured at a contracted state (e.g. end systole state) is the product of internal contraction forces generated from the relaxed state, the problem of reconstruction of these forces can be classified as an inverse problem. Ideally, this inverse problem should be formulated to resolve both the ischemic, and healthy contraction forces. However, such formulation leads to extremely ill-posed problem where obtaining a reasonably unique solution is very challenging. To reduce the ill-posedness of the problem, we follow a constrained reconstruction algorithm whereby we assume that the healthy, ischemic and infarct regions can be delineated from MRI or CT scans. This assumption is realistic as contrast enhanced MRI or CT imaging provide sufficient contrast for this delineation (So et al., 2018). We further assume that the contraction force within each region is uniformly distributed.

Figure 2-1 shows the flow chart of our proposed inversion technique which utilizes an optimization framework for the inversion. At its core, this technique involves a biomechanical model of the LV initialized at the relaxation state. This represents the problem's forward model where a volumetric distribution of contraction forces can be input to output the LV shape at end systolic contraction. These forces define what drive the contraction of the healthy, and damaged ischemic tissue. The end systolic shape of the model is then compared with the true shape of the segmented image at end systole using a cost function described in 2.3. The optimization algorithm then systematically adjusts the contraction force variables before being refed to the LV model to generate a new LV shape to compare until convergence is achieved. For optimization, a global optimizer was used which involves calculating the end systolic shape numerous times. To accelerate this

calculation a reduced model which involves a machine learning algorithm was developed. The following methodology describes each step of this inversion technique beginning with the LV model, then the cost function, and finally the global optimizer.
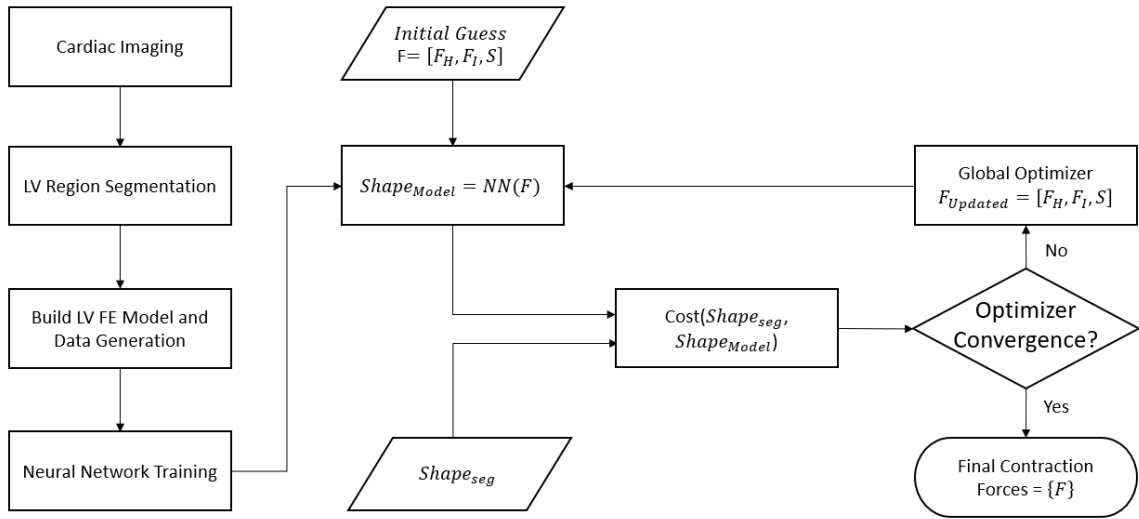
Figure 2-1. Flow chart for shape optimization technique.

2.2.2 « Biomechanical LV Model »

2.2.2.1 « Left Ventricle Models »

The purpose of biomechanical modelling in this optimization is to provide a bridge between the relaxed LV shape, and contracted LV shape using variable contraction forces. Two in-silico biomechanical models simulating different types of AMI damage are presented below in Figure 2-2. These models will be used to validate the proposed inversion technique. Each model is a finite element (FE) model inspired by an infarcted LV model developed by Haddad and Samani (Haddad & Samani, 2017a). In this model, the FE mesh is designed to have uniformly distributed nodes between the surfaces of two ellipsoids. The first model shown in Figure 2a, simulates the type of LV damage typical of a left anterior descending (LAD) coronary artery blockage. This is a common artery where patients experience AMI and will be referred to as the LAD model. The infarct area (white) propagates as a wave front into the tissue consistent with the literature in a semi spherical shape with a large surrounding periinfarct region (Reimer, Lowe, Rasmussen & Jennings, 2017). The second case in Figure 2b, simulates an infarction

caused by a blockage of the left circumflex (LC) coronary artery and will herein be referred to as the LC model. The infarct in this case is of a round shape penetrating transmurally from epicardium to endocardium in the midventricular area. It is surrounded by a large periinfarct region. Both models simulate an acute phase infarction where the periinfarct region is still damaged, and scar tissue has begun to form in the infarct area. The two cases with the different types of damage were chosen to evaluate different shapes and damages that a robust technique should be able to handle when recovering the myofiber contraction forces.
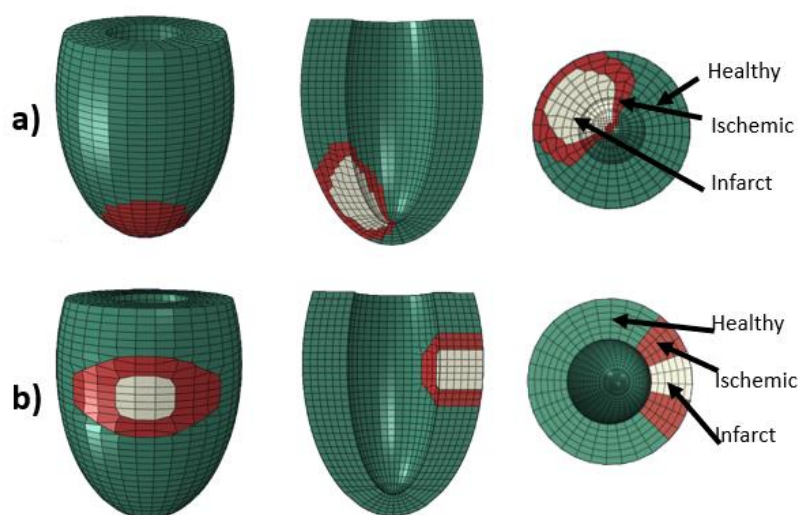
Figure 2-2. a) Finite element model of an infarcted LV, with a periinfarct region simulating AMI from the left anterior descending (LAD) coronary artery b) Finite element model of an infarcted LV, with a periinfarct region simulating AMI from the left circumflex (LC) coronary artery

2.2.2.2 « Geometry and Boundary Conditions »

The geometry of each model follows the mathematical description provided by Bovendeerd et al., 1992, simulating the LV of a canine. In the ischemic regions of each model, nodes in the model's FE mesh were moved to provide smooth surfaces at the interface of healthy, periinfarct, and infarct regions. In a clinical setting, the geometry would come from segmented volumes from a prior imaging session.

Boundary conditions of the proposed model are applied at the base of the LV where the LV would meet the left atrium and is considered a "fixed-in-plane" condition (Wang et al., 2014). Here we provide kinematic coupling, where the epicardial basal nodes can move radially but not rotationally. Also constrained are all base nodes to not move transverse to the basal plane. This mimics the LV being stuck in place as it is physiologically, but the muscle is free to contract and rotate from the apex up. It should be noted that more appropriate boundary conditions can be applied in a clinical setting. This includes boundary conditions at the left ventricle-right ventricle junction and data driven boundary conditions presented by Asner et al. 2017, which have proven to be more reliable for clinical simulation.

2.2.2.3 « Loading »

Following Haddad & Samani, 2017a, the LV myocardial tissue is modeled as a composite material with Hill's model used to incorporate the internal contraction generated by myofibers in the LV tissue. Hill's model contains two parallel components which are coupled when subjected to external or internal loading as illustrated in Figure 2-3a. The passive element represents the extracellular matrix (ECM) part of the LV tissue. The active element represents the myofibers with a resistance that accounts for the stiffness and passive response of the myofibers themselves. We employ these active elements as prestressed rebars penetrating the myocardial tissue volume. The orientation of these myofibers within the LV models are based on Streeter's canine data creating the known anisotropic contraction of the LV (Streeter et al., 1969). The advantage of these separate myofibers is that each one can be given a unique and controlled contraction as visible in Figure 2-3b. It is this property that allows us to assign different contraction forces to the separate regions of the LV models as well as different contraction characteristics within each element individually. The model also allows assigning different mechanical property parameters to the ECM and myofiber parts to account for pathological changes at the tissue microscopic level.
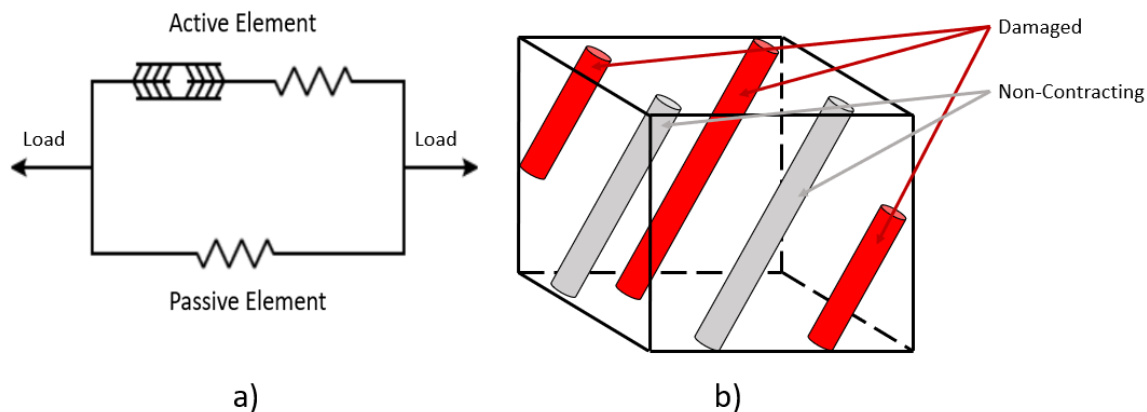
Figure 2-3. a) Hill's model, b) Rebar (myofiber) orientation

The first contraction force variable is that of healthy myocardial tissue which we denote as "F_H". This force can range from 140-160kPa consistent with the contraction range of myofibers found in the literature (Guccione & McCulloch, 1993). For the ischemic region, we introduce two variables to characterize contractility in the proposed model. The first variable represents the contraction force magnitude in the ischemic region which we denote as "F_I". It can range from 0kPa to the maximum healthy contraction force and is assigned to all myofibers in that region. This represents the possibly depressed contractility in the ischemic tissue. The second variable will be introduced as a tissue state variable "S" which represents the percentage of necrotic tissue. As AMI is being primarily tackled in this work, it is possible that some myocytes may be necrotic and by extension, some myofibers may be completely inactive. While these myofibers do not contract, they continue to contribute to the tissues passive response being volumetrically distributed. This state variable is considered to characterize such myofibers in the damaged tissue region. In the finite element model, this state describes the percentage of necrotic myofibers (rebars) uniformly distributed throughout each element in the ischemic region. It is noteworthy that the infarct region is assumed to be necrotic, hence no contraction forces are generated in that region.

The other loading necessary to properly capture the heart's physiology during systole is the surface pressure on the endocardium generated by the LV blood pool. This was

applied based on in-vivo measured data in canine left ventricles (Waldman, Nosan, Villarreal & Covel, 1998).

2.2.2.4   « Mechanical Properties »

In each tissue type involved in the LV model, there are 3 fundamental tissue mechanical properties that need to be defined. They pertain to the ECM of healthy myocardial tissue, the myofibers, and the pathological ECM of the infarct region. Hyperelastic strain energy density equations were used to define each material. The stress-strain data used in this work are obtained from Haddad and Samani (Haddad & Samani, 2017b) where in-silico uniaxial testing data was generated by the volume fraction and experimental stress-strain data of microconstituents of each tissue. The chosen hyperelastic models to fit this data were a 5th and 2nd order Ogden model. The 5th order model was used for the infarct LV myofibers and the infarcted ECM. The healthy background ECM and myofibers were modelled with a 2nd order Ogden model. Data of the hyperelastic parameters of each tissue can be found in (Haddad & Samani, 2017b).

As for the overall tissue volume distribution, the myofiber volume distribution is approximately 65% in the healthy and ischemic tissue (Schaper, Meiser & Stammler, 1985). In the infarct region, this percentage is reduced to approximately 5% as most myofibers are expected to have died in this time and, scar tissue replaces their volume (Bogatyryov, Tomanek, Dedkov, 2013).

To account for interpatient tissue stiffness variability of the above mechanical properties and to assess the impact of stiffness parameters deviation from average values reported in the literature, different stiffness characteristics were also considered. Using the reported average properties, we generated "softer" and "stiffer" tissue models for both the LAD and LC models. The softer tissue model was generated to achieve 20% stiffness reduction compared to the stiffness obtained using the experimental data reported in literature, while the stiffer tissue model was generated to achieve 20% stiffness increase. The inversion technique was tested between models of varying stiffnesses to determine whether the algorithm is sensitive to the interpatient variability of mechanical properties.

While mechanical properties can be optimized for, the ability to use average values significantly reduces the cost and complexity.

2.2.3 « Cost Function »

As described earlier, the constrained contraction force reconstruction problem used in this work is solved using optimization. With the biomechanical model in place, we now describe the cost function to minimize the shape difference between both the model, and segmented shape. Since a goal of this technique is to offer an algorithm which is free of tissue motion tracking, we propose to use the similarity of the two contracted shapes alone. This can be done using a variety of similarity metrics such as Hausdorff distance, landmark based error, or the root mean squared error (RMSE). Hausdorff distance is appealing but is computationally expensive to run in an iterative solver. Landmark based error requires manual entry of landmarks, and again, required more steps. RMSE however is computationally inexpensive and considers the segmented shape and model output directly with no intervention and was thus chosen as the cost function as follows:

$$Cost = RMSE(LV_{seg}, LV_{Model}(F)) \qquad\qquad (1)$$

where F denotes the contraction force parameters and state variable and the Cost function has an ideal minimum value of 0. Given that the model and image segmentation may not be registered, iterative closest point (ICP) was performed as an automatic rigid registration algorithm. ICP also outputs RMSE which is required. Since the present study involves an in-silico model, the segmented shape will be generated by the LAD and LC models themselves. This alone is unrealistic in the context of clinical applications as when biomechanical modelling is performed with real patient geometry, there will be segmentation errors, modelling errors caused by the computation, as well as errors caused by different image resolution. To account for these errors, we systematically altered the contracted LV shape obtained from forward FE model. For this purpose, the shape was scaled randomly from 0 to 5%, subjected to shearing consistent with 5 to 12 degrees, and finally, the nodal data was down sampled to approximately 50% of available information.

2.2.4 « Global Optimizer »

To minimize this multi-variable cost function consisting of the healthy contraction F_H, ischemic contraction F_I and the ischemic state S, genetic algorithms (GA) were used to find the global minimum. The GA was chosen out of a large selection of optimization algorithms for its effectiveness in finding the global minimum compared to other optimization techniques. In this work, the GA ran for 300 generations with a population of 50, unless each population stalled. This number of iterations can total 15000, and since FE modelling is computationally expensive taking on average 3.5 minutes to run each iteration, steps to decrease the computational cost were taken as described in the next section.

2.2.4.1 « Neural Network Training and Principal Component Reduction »

To improve the computational efficiency of our proposed technique, we developed a reduced model to substitute the FE model of the LV. This reduced model includes a neural network (NN) which was trained using data obtained from running the FE model of the LV with various stiffness and contraction force sets of parameters. The sets of parameters used to generate the training data sampled the space sufficiently. After training, each NN takes as input the 3 contractility variables of F_H, F_I and S and outputs the LV model shape, skipping the normally required steps in between start and end geometry required in FE analysis. Each network is a 3-layer neural network with tan-sig transfer functions for the first 3 layers and a linear transfer function to the output deformed LV shape shown in Figure 2-4. This is a network configuration that has been validated in previous studies of statistical shape optimization of FE prostates (Mousavi et al., 2012). In this study, the authors express that the applied technique is general to any properly noded mesh which is why its robust methodology was applied.
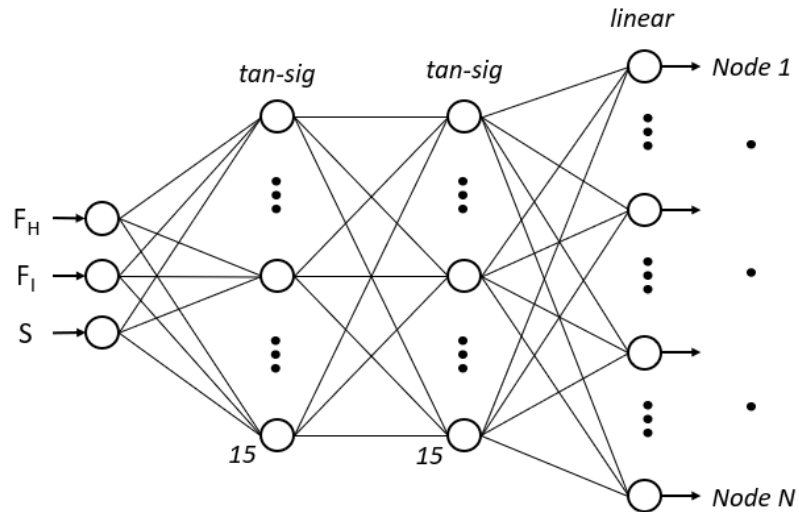
Figure 2-4. Topology of the neural network (PCrNN) developed as a reduced biomechanical model of the LV

To employ this 3-layer NN as an efficient replacement to the accurate biomechanical model of the LV, it was necessary to express the LV displacement field in a mathematically compact form. Similar to (Mousavi et al., 2012), this was achieved by breaking down the displacement data into its principal components creating a principal component reduced neural network (PCrNN).

To train each PCrNN, 1100 training data sets containing the displacement of LV nodes on the endocardium and epicardium were generated for each LV case. This training took approximately 3 days for each network, but when employed within the developed GA, the optimization was reduced from an estimated 140 days to 20 minutes on a regular I7 desktop, which puts this technique in the range of clinical applications.

2.2.5 « Validation of the Proposed Technique »

We tested the effectiveness of the technique by providing a variety of contracted shapes to our algorithm. The contracted shapes were generated by changing the 3 variables in our biomechanical FEM model, F_H, F_I, and S at random. For each biomechanical model, LAD and LC, 5 cases were generated for the proposed methodology. The 5 cases involved shape data corresponding to displacement fields generated with 3 different sets

of variables representing various *healthy contractions, damaged tissue contractions, and percentage of non-contracting myofibers* in both the LAD and LC LV models. The true values are shown in table 2-1. These data sets were combined with errors representing segmentation and model errors as described earlier to generate more realistic LV shapes anticipated with clinical data.

Table 2-1 Test cases for shape optimization technique

LAD Test Cases	F_H (kPa)	F_I (kPa)	S (% activity)
Case 1	157	40	0
Case 2	155	100	0
Case 3	154	70	60
Case 4	150	70	40
Case 5	155	92	60
LC Test Cases	F_H (kPa)	F_I (kPa)	S (% activity)
Case 1	144	75	20
Case 2	150	100	0
Case 3	143	71	80
Case 4	154	46	40
Case 5	159	127	20

To account for stiffness uncertainties in the proposed reconstruction technique, as indicated earlier, shape data were generated using LV models with lower stiffness (soft model) and higher stiffness (stiff model) than the reference stiffness characteristics. For each case we generated a contracted shape using the soft model and ran it through the stiff model solver; we then ran a different stiff contracted shape through the soft solver.

We present the error of the ischemic contraction F_I relative to the magnitude of healthy contraction F_H. This is because the focus of this technique is to determine the amount of salvageable myofiber contraction. For instance, 10kPa vs 20kPa is a 100% difference, but when compared to a healthy contraction of 155kPa, we see 6% contraction vs 13% where, in both cases, large recovery would be expected.

2.3 « Results »

2.3.1   « Model Function »

The LV biomechanical model presented in this article was previously validated in
(Haddad & Samani, 2017a). We present in Figure 2-5 example contracted LVs for both
the LAD and LC models. For both models F_H was set to 150kPa, F_I set to 50% of healthy
contraction, and S set to 0%. This figure shows what should be expected of a realistic
model including wall thickening in the healthy myocardium as seen in the long axis view,
as well as wall thinning, torsion, and minimal deformation in the infarct area shown in
the short axis section of each model.
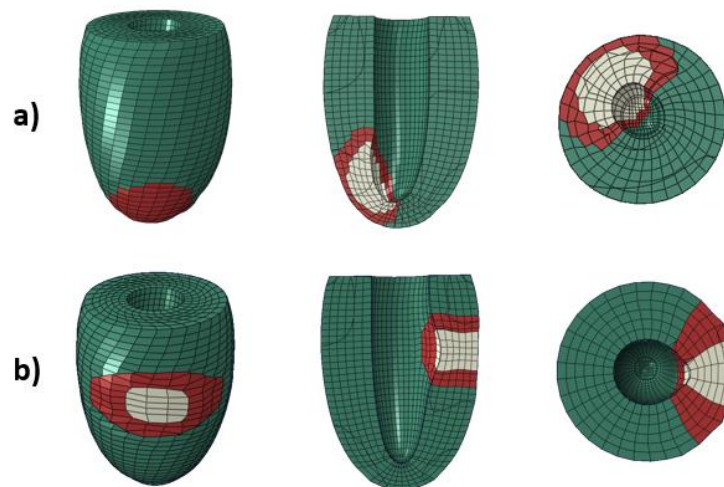
Figure 2-5. a) Finite element model of the contracted LAD model and b) Finite element
model of the contracted LC model both under $F_H = 150$kPa, $F_I = 75$kPa and $S = 0$.

In Figure 2-6 we again show the two models but with different contraction forces than the
above. Here, we set F_H to 142kPa, F_I set to 85% of healthy contraction, and S set to 10%.
Between both figures the shape differences are evident through visual inspection. Results
obtained with the data generated for the 5 cases described in the Methods are presented in
the next section.
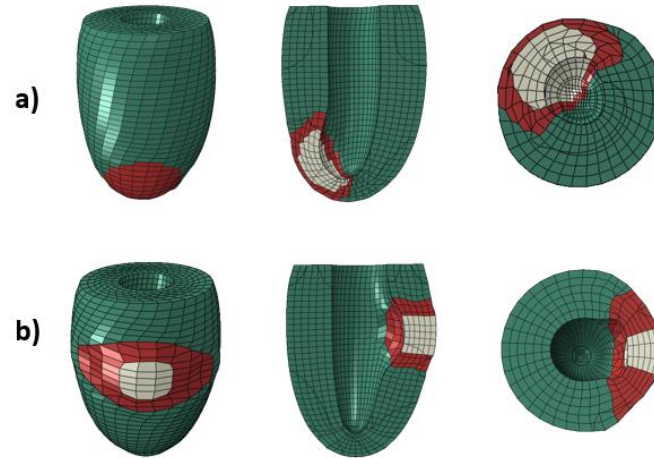
Figure 2-6. a) Finite element model of the contracted LAD model b) Finite element model of the contracted LAD model both under $F_H = 142kPa$, $F_I = 120.7kPa$ and $S = 10\%$.

2.3.2 « Optimization Results for LAD and LC Left Ventricles »

Presented are the proposed technique's optimization results obtained for the LAD and LC infarcted LV models for the 5 cases. Figures 2-7 and 2-8 contain the results for the LAD and LC models, respectively.
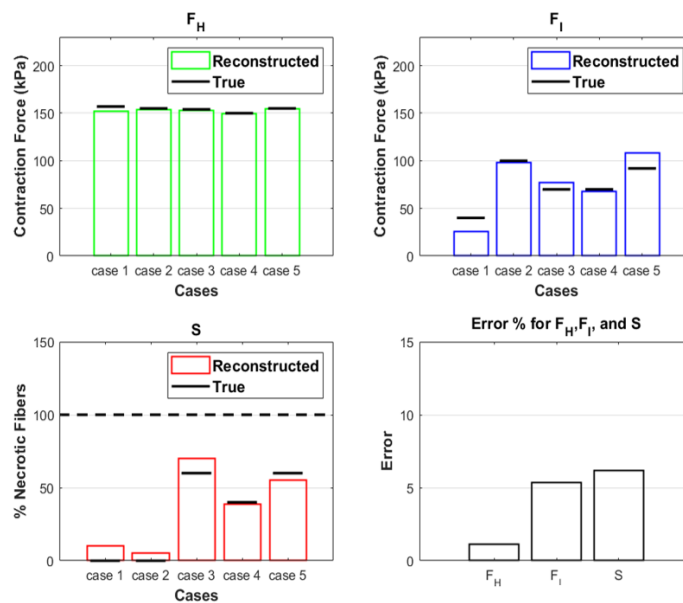
Figure 2-7. Reconstruction results for LAD model cases with mean error reported
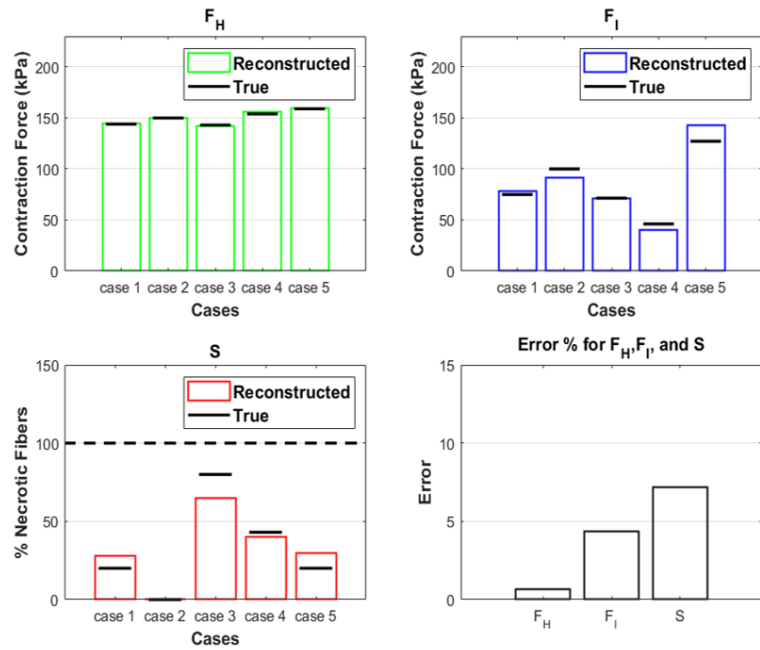
Figure 2-8. Reconstruction results for LC model cases

As indicated in the Methods, shape data generated with "softer" and "stiffer" scenarios were generated in conjunction with a LAD and LC models before they were used as input in the proposed reconstruction algorithm. Combined in Figure 2-9 are the results corresponding to these models.
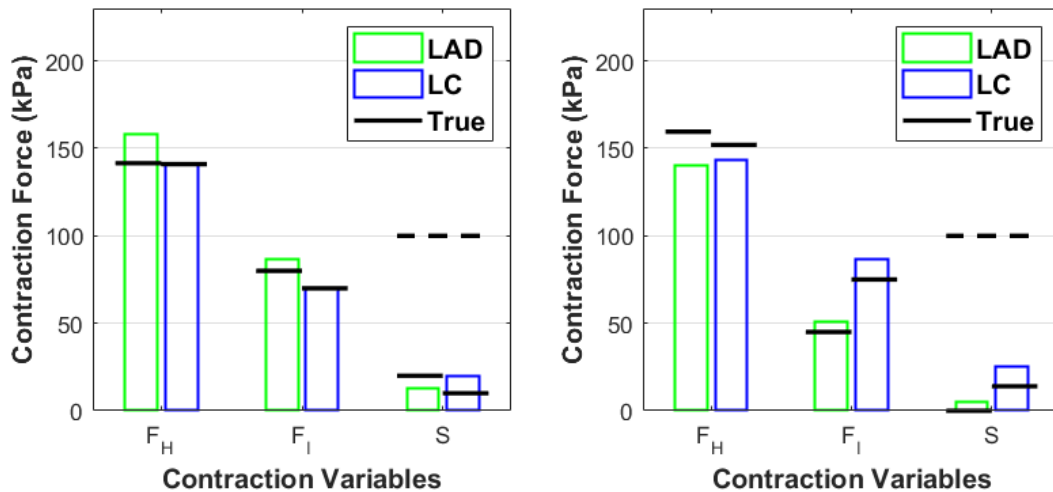
Figure 2-9. Reconstruction results for the soft model in stiff solver (left) and stiff model in soft solver (right).

We summarize the results of the shape optimization technique in Table 2-2. It shows the error of the reconstruction technique for each model and stiffness individually, and then total error for each variable at the bottom.

Table 2-2 Reconstruction results for the "softer" and "stiffer" models run in each other for the LAD model.

	F_H Error		F_I Error		S Error	
	Normal	**Soft/Stiff**	**Normal**	**Soft/Stiff**	**Normal**	**Soft/Stiff**
LAD	1%	12.8%	5.3%	3%	6.2%	6%
LC	1%	9.9%	4.3%	6.9%	7.2%	10.5%
	F_H Error		F_I Error		S Error	
Overall Error	3.6%		4.9%		7.1%	

2.4 « Discussion and Conclusions »

For patients who suffer from AMI, imaging is a necessary step in determining the extent of tissue damage. Imaging modalities (e.g. CT, MRI or SPECT) can provide information on the location and extent of permanently damaged and salvageable myocardial tissue. However, they lack quantitative functional information of the myofibers themselves, hence may not be sufficient for deciding a proper course of treatment if follow up imaging is delayed. We proposed a novel technique which can use imaging in conjunction with a biomechanical model of the LV that provides quantitative functional tissue information that could potentially improve the prognosis of AMI patients. The acquirable information we present is the general magnitude of myofiber contraction forces in the healthy and ischemic regions including a state variable for non-contracting myofibers which can be used to predict final infarct volume.

The proposed method reconstructs these important parameters through optimizing a biomechanical model of the LV to best fit the contracted shape of the segmented LV of the patient. This technique was developed to avoid costly methods of tissue motion tracking (e.g. MRI tagging, MRI phase imaging) at a cost to heterogeneity. By avoiding this need, we make the clinically available and cost-effective CT imaging for use in cardiac biomechanical modelling. While currently a less popular choice in heart disease diagnosis due to dose considerations, CT imaging is increasing in popularity in the heart diagnosis field for this purpose due to advancements in perfusion imaging and fast, full, volumetric coverage. As such, CT imaging-based techniques can be potentially a clinically viable option. The technique only requires the geometry of the LV at its relaxed state and a contracted state with delineable infarct regions as input to find the best force distribution that lead to the best matching of the contracted shape. As mentioned in the introduction, the delineable infarct region may not be the true representation. This can be overcome with modelling as well, by introducing perturbations to the delineated borders lead to the best cost function and agreement with the total heart shape.

This technique was tested with two in-silico models of a LV suffering AMI, including a LAD AMI and an LC AMI events. In the LAD model, the tissue contraction values were predicted within errors less than 1% for healthy tissue, 5.3% for damaged ischemic tissue, and 6.2% for non-contracting candidates. For the LC model, the errors were 1%, 4.3% and 7.2% for the healthy, damaged, and non-contracting candidates, respectively. The numerical experiments performed to account for tissue stiffness estimation errors relative to average values reported in the literature indicated that similar accuracy can be achieved. This implies that the sensitivity of the proposed technique to uncertainties in the tissue stiffness parameters is not substantial, therefore, average patient mechanical properties available in the literature can be used.

With this range of error, the proposed method can be potentially used in a very interesting clinical applications such assessment of cardiac function recovery under various scenarios before deciding a proper course of treatment. For such assessment, a first step would be to use the reconstructed contraction forces in conjunction with estimated errors to predict best and worse case scenarios for patient specific functional recovery.

Following the pathology of MI after its onset, non-contracting myofibers identified using this technique can be replaced with scar tissue or removed from the model altogether with simulated wall thinning (Shah et al., 2013). The output of this model would give a worst-case scenario for ejection fraction and possibly predicting potential cardiac remodeling. Opposite to this scenario is to assume those fibers heal along with the rest of the viable tissue and look at the best-case scenario. Since recovery of revascularized tissue can take up to a year, intermittent imaging using any major imaging modality that provides geometry may also have to accompany this assessment to better assess the state of recovery. An interesting application of such patient specific information is to help decide which AMI patients should be placed on heart transplant lists and which ones need invasive revascularization surgery (for example, coronary artery bypass graft surgery) urgently. If massive necrotic damage is predicted, clinicians would be able to act sooner than waiting for the tissue to conform to its final shape while also saving the cost of a follow up imaging session.

The average time to optimize one case using the proposed technique run on a regular I7 computer desktop is approximately 20 minutes. This means that valuable diagnostic results can be generated and delivered to the physician before devising a course of action in a reasonable amount of time. This time does not include LV segmentation; however, this is not a significant limiting factor as many effective LV automatic segmentation methods have been developed recently (Avendi, et. al., 2016). It is noteworthy that the computation process can be accelerated using parallel computing, leading to availability of diagnostic information even in seconds. Combining the information obtained from the contraction parameter reconstruction with biomechanical modelling also offers the added benefit of computation of stress in the LV. This information could be used in other predictive models such as information for mechanotransduction in cardiac remodelling or implicate the future thickening of the LV as the LV optimizes its function over time (Sutton & Sharpe, 2000).

In the proposed technique, individual-based PCrNN was utilized to accelerate the optimization process. This requires the patient specific geometry of the LV to develop and train the NN. Another potential option to avoid the step of PCrNN involves the

development of a population based NN where, in addition to the contraction force parameters, a PCA based parameterized geometry of the LV is also required as input. In that case a more sophisticated NN trained using a larger dataset would be required. Acquisition of such dataset is quite feasible as it only requires availability of numerous cardiac CT scans of AMI patients.

In this in-silico study, the employed RMSE cost function optimization included an average cost function value of 2.5mm which accounts for segmentation and modelling errors and is likely to be an underestimation. To enhance the method's performance, the cost function may be modified to use more image information such as wall thickness and simple strain estimations. This may allow a higher level of heterogeneity in our model, allowing for more contraction force variables. It's unclear how much heterogeneity is required for clinical use as the field is still in its infancy. Coarse regional estimations like the models presented may be all that is required. The feasibility of very heterogenous contraction force reconstruction does exist. Finsberg, et. al. 2018 have recently proposed an adjoint gradient based method for determining the contractility in LV's with over 1700 contraction variables, this was possible with more resolved data provided by tissue motion tracking. This model however, had one myofiber per element, whereas we install approximately 60 myofibers per element which allowed us to explore the non-contracting state, a previously unexplored option which is not possible with single fiber modelling. With our model, the passive stiffness of the myocardial tissue which expresses itself in the final shape, is related to the fibers that may be extremely damaged, not just pre-set mechanical properties. This is a new distinction that may have prognostic value in the clinic.

The proposed technique is also extendable to predict the mechanical properties of the LV. Using the end diastolic shape, the neural network could optimize the blood pressure with mechanical properties of ECM monitoring diseases such as amyloidosis (Bhupathi, Shalasani & Rokey, 2011).

« References »

1. Asner, L., Hadjicharalambous, M., Chabiniok, R., Peressutti, D., Sammut, E., Wong, J., … Nordsletten, D. (2017). Patient-specific modeling for left ventricular mechanics using data-driven boundary energies. *Computer Methods in Applied Mechanics and Engineering*, *314*, 269–295.

2. Asner, L., Hadjicharalambous, M., Chabiniok, R., Peresutti, D., Sammut, E., Wong, J., … Nordsletten, D. (2016). Estimation of passive and active properties in the human heart using 3D tagged MRI. *Biomechanics and Modeling in Mechanobiology*, *15*(5), 1121–1139.

3. Avendi, M. R., Kheradvar, A., & Jafarkhani, H. (2016). A combined deep-learning and deformable-model approach to fully automatic segmentation of the left ventricle in cardiac MRI. *Medical Image Analysis*, *30*, 108–119.

4. Balaban, G., Finsberg, H., Funke, S., Håland, T. F., Hopp, E., Sundnes, J., … Rognes, M. E. (2018). In vivo estimation of elastic heterogeneity in an infarcted human heart. *Biomechanics and Modeling in Mechanobiology*, *17*(5), 1317–1329.

5. Balaban, G., Finsberg, H., Odland, H. H., Rognes, M. E., Ross, S., Sundnes, J., & Wall, S. (2017). High-resolution data assimilation of cardiac mechanics applied to a dyssynchronous ventricle. *International Journal for Numerical Methods in Biomedical Engineering*, *33*(11), 1–17.

6. Benjamin, E. J., Virani, S. S., Callaway, C. W., Chamberlain, A. M., Chang, A. R., Cheng, S., … Muntner, P. (2018). *Heart disease and stroke statistics - 2018 update: A report from the American Heart Association*. *Circulation* (Vol. 137). https://doi.org/10.1161/CIR.0000000000000558

7. Bhupathi, S. S., Chalasani, S., & Rokey, R. (2011). Stiff heart syndrome. *Clinical Medicine and Research*, *9*(2), 92–99.

8. Bogatyryov, Y., Tomanek, R. J., & Dedkov, E. I. (2013). Structural Composition of Myocardial Infarction Scar in Middle-aged Male and Female Rats: Does Sex Matter? *Journal of Histochemistry and Cytochemistry*, *61*(11), 833–848.

9. Bovendeerd, P. H. M., Arts, T., Huyghe, J. M., van Campen, D. H., & Reneman, R. S. (1992). Dependence of local left ventricular wall mechanics on myocardial fiber orientation: A model study. *Journal of Biomechanics*, *25*(10), 1129–1140.

10. Camici, P. G., Prasad, S. K., & Rimoldi, O. E. (2008). Stunning, hibernation, and assessment of myocardial viability. *Circulation*, *117*(1), 103–114.

11. Chabiniok, R., Moireau, P., Lesault, P. F., Rahmouni, A., Deux, J. F., & Chapelle, D. (2012). Estimation of tissue contractility from cardiac cine-MRI using a biomechanical heart model. *Biomechanics and Modeling in Mechanobiology*, *11*(5), 609–630.

12. Fernández-Jiménez, R., Sánchez-González, J., Agüero, J., García-Prieto, J., López-Martín, G. J., García-Ruiz, J. M., … Ibáñez, B. (2015). Myocardial edema after ischemia/reperfusion is not stable and follows a bimodal pattern: Imaging and histological tissue characterization. *Journal of the American College of Cardiology*, *65*(4), 315–323.

13. Finsberg, H., Balaban, G., Ross, S., Håland, T. F., Odland, H. H., Sundnes, J., & Wall, S. (2018). Estimating cardiac contraction through high resolution data assimilation of a personalized mechanical model. *Journal of Computational Science*, *24*, 85–90.

14. Genet, M., Chuan Lee, L., Ge, L., Acevedo-Bolton, G., Jeung, N., Martin, A., … Guccione, J. M. (2015). A Novel Method for Quantifying Smooth Regional Variations in Myocardial Contractility Within an Infarcted Human Left Ventricle Based on Delay-Enhanced Magnetic Resonance Imaging. *Journal of Biomechanical Engineering*, *137*(8), 081009.

15. Guccione, J. M., & McCulloch, A. D. (1993). Mechanics of Active Contraction in Cardiac Muscle: Part I—Constitutive Relations for Fiber Stress That Describe Deactivation. *Journal of Biomechanical Engineering*, *115*(1), 72–81.

16. Haddad, S. M. H., & Samani, A. (2017a). A computational model of the left ventricle biomechanics using a composite material approach. *International Journal of Engineering Science*, *111*, 61–73.

17. Haddad, S. M. H., & Samani, A. (2017b). A novel micro-to-macro approach for cardiac tissue mechanics. *Computer Methods in Biomechanics and Biomedical Engineering*, *20*(2), 215–229.

18. Hadjicharalambous, M., Asner, L., Chabiniok, R., Sammut, E., Wong, J., Peressutti, D., … Nordsletten, D. (2017). Non-invasive Model-Based Assessment of Passive Left-Ventricular Myocardial Stiffness in Healthy Subjects and in Patients with Non-ischemic Dilated Cardiomyopathy. *Annals of Biomedical Engineering*, *45*(3), 605–618.

19. Karabelas, E., Gsell, M. A. F., Augustin, C. M., Marx, L., Neic, A., Prassl, A. J., … Plank, G. (2018). Towards a computational framework for modeling the impact of aortic coarctations upon left ventricular load. *Frontiers in Physiology*, *9*(MAY), 1–20.

20. Kelly, R. F., Cabrera, J. A., Ziemba, E. A., Crampton, M., Anderson, L. B., McFalls, E. O., & Ward, H. B. (2011). Continued depression of maximal oxygen consumption and mitochondrial proteomic expression despite successful coronary artery bypass grafting in a swine model of hibernation. *Journal of Thoracic and Cardiovascular Surgery*, *141*(1), 261–268.

21. Kim, R. J., Wu, E., Rafael, A., Chen, E.-L., Parker, M. A., Simonetti, O. P., … Judd, R. M. (2000). The Use of Contrast-Enhanced Magnetic Resonance Imaging to Identify Reversible Myocardial Dysfunction. *New England Journal of Medecine*, *343*(20), 1445–1453.

22. Larghat, A. M., Maredia, N., Biglands, J., Greenwood, J. P., Ball, S. G., Jerosch-Herold, M., … Plein, S. (2013). Reproducibility of first-pass cardiovascular magnetic resonance myocardial perfusion. *Journal of Magnetic Resonance Imaging*, *37*(4), 865–874.

23. Mor-Avi, V., Lang, R. M., Badano, L. P., Belohlavek, M., Cardim, N. M., Derumeaux, G., … Zamorano, J. L. (2011). Current and evolving echocardiographic techniques for the quantitative evaluation of cardiac mechanics: ASE/EAE consensus statement on methodology and indications endorsed by the Japanese society of echocardiography. *European Journal of Echocardiography*, *12*(3), 167–205.

24. Mousavi, S. R., Khalaji, I., Naini, A. S., Raahemifar, K., & Samani, A. (2012). Statistical finite element method for real-time tissue mechanics analysis. *Computer Methods in Biomechanics and Biomedical Engineering*, *15*(6), 595–608.

25. Nayak, K. S., Nielsen, J. F., Bernstein, M. A., Markl, M., Gatehouse, P. D., Botnar, R. M., … Raman, S. V. (2015). Cardiovascular magnetic resonance phase contrast imaging. *Journal of Cardiovascular Magnetic Resonance*, *17*(1), 1–26.

26. Nikou, A., Dorsey, S. M., McGarvey, J. R., Gorman, J. H., Burdick, J. A., Pilla, J. J., … Wenk, J. F. (2016). Effects of using the unloaded configuration in predicting the in vivo diastolic properties of the heart. *Computer Methods in Biomechanics and Biomedical Engineering*, *19*(16), 1714–1720.

27. Norum, I. B., Ruddox, V., Edvardsen, T., & Otterstad, J. E. (2015). Diagnostic accuracy of left ventricular longitudinal function by speckle tracking echocardiography to predict significant coronary artery stenosis. A systematic review. *BMC Medical Imaging*, *15*(1).

28. Pasque, M. K. (2017). Not all that hibernates necessarily wakes up. *Journal of Thoracic and Cardiovascular Surgery*, *153*(3), 591–592.

29. Reimer, K. A., Lowe, J. E., Rasmussen, M. M., & Jennings, R. B. (2017). The Wavefront Phenomenon of Ischemic Cell Death 1. Myocardial Infarct Size vs Duration of Coronary Occlusion in Dogs Downloaded from, 786–794. Retrieved from http://circ.ahajournals.org/

30. Schaper, J., Meiser, E., & Stammler. (1985). Ultrastructural morphometric analysis of myocardium from dogs, rats, hamsters, mice, and from human hearts. *Circulation Research*, *56*(3), 377–391.

31. Shah, D. J., Kim, H. W., James, O., Parker, M., Wu, E., Bonow, R. O., … Kim, R. J. (2013). Prevalence of regional myocardial thinning and relationship with myocardial scarring in patients with coronary artery disease. *JAMA - Journal of the American Medical Association*, *309*(9), 909–918.

32. So, A., Wisenberg, G., Teefy, P., Yadegari, A., Bagur, R., Hadway, J., … Lee, T. Y. (2018). Functional CT assessment of extravascular contrast distribution volume and myocardial perfusion in acute myocardial infarction. *International Journal of Cardiology*, *266*, 15–23.

33. Streeter, D. D., Patel, D. P., Spotnitz, H. M., Ross, J., & Sonnenblick, E. H. (1969). Fiber Orientation in the Canine Left Ventricle during Diastole and Systole. *Circulation Research*, *24*(3), 339–347.

34. Sutton, M. G., & Sharpe, N. (2000). Left ventricular remodeling after myocardial infarction: pathophysiology and therapy. *Circulation*, *101*(25), 2981–2988.

35. Waldman, L. K., Nosan, D., Villarreal, F., & Covell, J. W. (1988). Relation between transmural deformation and local myofiber direction in canine left ventricle. *Circulation Research*, *63*(3), 550–562.

36. Wang, H. M., Luo, X. Y., Gao, H., Ogden, R. W., Griffith, B. E., Berry, C., & Wang, T. J. (2014). A modified Holzapfel-Ogden law for a residually stressed finite strain model of the human left ventricle in diastole. *Biomechanics and Modeling in Mechanobiology*, *13*(1), 99–113.

37. World Health Organization. (2017, May 17). *Cardiovascular diseases (CVDs).* Retrieved from https://www.who.int/news-room/fact-sheets/detail/cardiovascular-diseases-(cvds) Accessed: August 13th, 2019

38. Wright, J., Adriaenssens, T., Dymarkowski, S., Desmet, W., & Bogaert, J. (2009). Quantification of Myocardial Area at Risk With T2-Weighted CMR. Comparison With Contrast-Enhanced CMR and Coronary Angiography. *JACC: Cardiovascular Imaging*, *2*(7), 825–831.

Chapter 3

3 « A Composite Material Based Neural Network for Tissue Mechanical Properties Estimation Toward Stage Assessment of Infarction »

3.1 « Introduction »

Acute myocardial infarction (AMI) is a product of cardiovascular disease, the leading cause of death worldwide [1]. For patients who have suffered AMI, prognostic medicine is required for treatment planning and monitoring of patients. This prognosis is variable among patients and depends highly on factors such as the extent of infarct and the residual functionality (i.e. contractility) [2]. Recent research in biomechanical modelling has shown the ability to model the mechanics of diseased hearts which can be used as a tool to enrich our knowledge on the pathophysiological changes that present themselves post myocardial infarction [3]. These changes include alteration of tissue mechanical properties in the scar region, loss of contractility in the infarct core and border regions, as well as remote remodeling due to new stress concentrations in the myocardium [3].

To obtain accurate, biomechanical model based prognostic information required in Chapter 2, the geometry, loading, boundary conditions, and mechanical properties must be personalized to the patient. Among them, personalized mechanical properties of healing scar tissue can be of special interest due to their potential in providing prognostic information to better guide the patients' therapies [4]. An effective way to glean out valuable diagnostic data using cardiac mechanics models involves using them as a forward model within an inverse problem framework where data pertaining to a medical test (e.g. cardiac MRI or CT image) is inverted to obtain diagnostic data (e.g. contraction forces as well as personalized tissue mechanical properties). For setting up an inverse problem framework involving personalized mechanical parameters of healing scar tissue, however, poses a computational problem wherein heterogenous modelling increases the complexity tremendously. Commonly, mechanical properties are defined with

hyperelastic strain energy density functions, the most common being the 8 variable Holzapfel-Ogden model [5]. Clearly, 8 variables per tissue type in the model is a large requirement in the context of inverse problem formulation which typically involves hundreds, or thousands runs of the forward model before data reconstruction is made available.

To reduce the complexity, a common approach is to use population-based parameters optimized from experimental myocardial stress vs strain data for less sensitive variables. An alternative is to use simplified models of the Holzapfel-Ogden equation considering tissue transverse isotropy [6]. These techniques are widely adopted and allow heterogenous modelling of various heart pathologies. One issue with this approach well discussed in [6] is the non-uniqueness of most hyperelastic strain energy density equations. While the parameter set itself allows accurate modelling, they have little value as biomarkers.

Recently, another approach has been suggested to predict the mechanical properties of healthy and pathologic cardiac tissue which is based on composite materials. In Haddad & Samani, the healthy myocardium was simulated as a 4-variable construct of its micro constituents (myofibers, collagen, fibroblasts, and myocytes) [7]. This approach was successful in showing that the mechanical properties of myocardial tissue is a function of volume and intrinsic properties of its microconstituents. Models developed using the composite material approach have accurately predicted observations reported in the literature for both healthy and mature infarct tissue.

This micro-to-macro approach has valuable applications for patients undergoing the healing stages of AMI which takes place over approximately 8 weeks where knowledge of the percentage of these microconstituents can be extremely valuable. For instance, determining whether there is high risk of rupture due to low collagen content [8]. There is also plenty of research on how the percentage of these micro constituents change in time during the healing period. Within an inverse optimization framework, a highly efficient function such as neural network that can predict mechanical properties based on a single parameter, we introduce to indicate healing stage would be very effective. Central to this

work is development of such function using relevant population-based data pertaining to microconstituents of scar tissue in various healing stages.

Presented here, is an approach we propose to predict the mechanical properties of myocardial tissue ranging from healthy tissue to mature scar. We hypothesize that compiled literature of the micro constituents of infarct tissue in time post myocardial infarction can be used to predict the stage of patient specific infarct healing while also predicting new cardiac biomarkers. We show the concept behind developing a library of healing scar tissue mechanical properties for use in modelling and staging. This approach reduces the multivariable optimization traditionally used to obtain scar tissue mechanical properties to a single variable representing the stage in the MI healing process. In addition, the proposed approach provides estimates of patient-specific volume percentages of the scar tissue micro constituents which can be used as new biomarkers with prognostic clinical value. In this paper, preliminary whole tissue mechanical properties are obtained for a tissue model under uniaxial testing conditions and the generated predictive network is evaluated.

3.2 « Methodology »

3.2.1 « Overview »

Building the mechanical property library for the scar tissue during healing process can be broken down into 3 steps shown in Fig 3-1. First presented is the simulated uniaxial testing of cardiac tissue composite material using the FE model described in 3.2.2. Second, is using this FE model to generate the predicted stress-strain data for time-varying concentrations of the microconstituents as described in 3.2.3. The last step is building a predictive neural network allowing estimation of the mechanical properties as a continuous function of time during the scar formation process as described in 3.2.4.
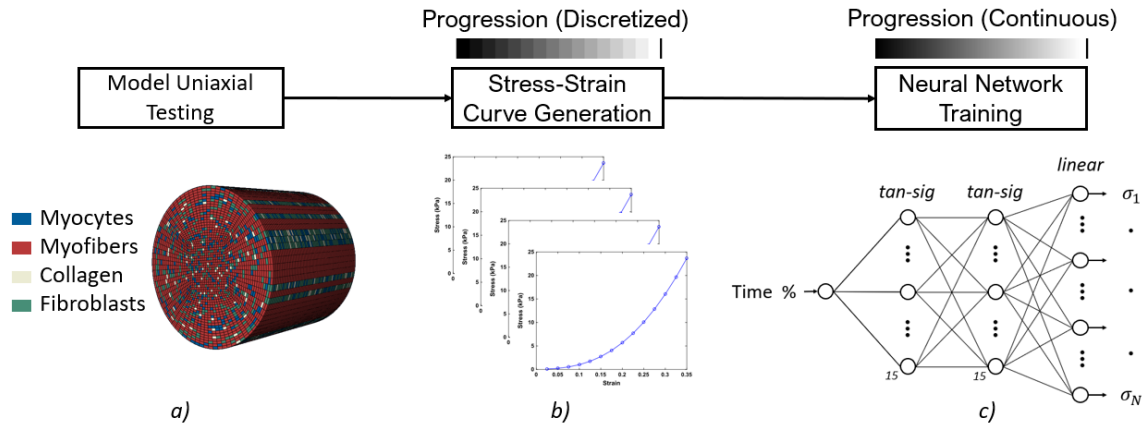
Figure 3-1 Finite element composite material model of scar tissue (a); Generating time-varying stress-strain curves of scar tissue (b); Fitting an NN for scar tissue stress-strain curve as a function of scar progression time (c).

3.2.2   « Scar Tissue Model »

The scar tissue model used for simulating uniaxial testing is a cylinder geometry built of hexahedral elements as shown in Fig 1a). This composite material model allows controlling the percentage volume of the micro constituents. In Haddad and Samani, 4 microconstituents of collagen, myofibers, fibroblasts, and myocytes were considered to comprise the volume of a typical myocardial tissue. Since 95% of myocytes' volumes are mitochondria, they represented the myocytes as mitochondria with known stiffness. All constituents were modelled with Yeoh hyperelastic strain energy density functions with their values reported in [7]. The myofibers were installed to longitudinally penetrate the tissue in the cylinder, and the rest of the micro constituents were randomly distributed within the tissue according to the literature.

To simulate tension or compression under uniaxial testing using FE modeling and shown visually in Fig. 3-2, one side of the cylinder was subject to a displacement boundary condition, while the opposite side of the cylinder is subject to a "fixed in plane" boundary condition where the tissue can move transverse to the tension or compression. To prevent rotation, two nodes were subject to x-axis symmetry while the displacement of another two nodes were y-axis symmetrical. The reaction force post simulation at each

applied strain was then obtained and divided by the true area to obtain the stress-strain curve.
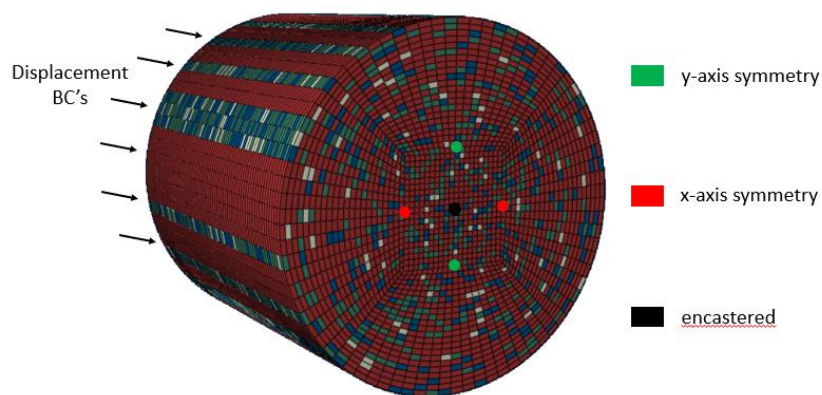
Figure 3-2 Schematic of the uniaxial finite element simulation of cardiac tissue.

3.2.3 « Modelling Scar Healing »

The purpose here is to generate stress-strain curves of the scar tissue model at several discrete time points throughout the healing process. Key for achieving this purpose is estimating the scar tissue microconstituents and their percentages at each time point. Generally, scar healing is divided into three stages, the inflammatory stage, proliferative stage, and maturation stage [9]. In the inflammatory stage, there is myofiber necrosis formation which takes place over ~7 days accompanied by edema, and collagen break down which allows future fibroblast migration. In the proliferative stage, fibroblasts fill the interstitial space depositing collagen and building the new infarct extracellular matrix as the collagen cross-linking increases. Finally, in the maturation stage, the fibroblast population decreases, and the collagen cross linking continues.

The mechanical properties of cardiac tissue are most dependent on the percentage volume of collagen since it has the highest stiffness among the micro constituents. Based on the available literature on collagen concentration post myocardial infarction, a modified Fermi-Dirac function in equation 3-1 below was fit to describe the increase in collagen during scar healing [10-13].

$$C(t) = \frac{a}{1+\exp\left[\frac{t-b}{c}\right]} + d \qquad\qquad (3\text{-}1)$$

The coefficients *a,b,c,d* are used to provide flexibility to the fit, and C(t) is the collagen concentration, and *t* is the time.

This factor function is shown in Fig 3-3. The myofiber percentage is known to drop during the inflammatory stage from a typical 67% volume in healthy tissue down to ~5% [7]. This was captured by a 2-term exponential function which decayed to 5% on 7 days and then held steady. During the inflammatory stage, edema was modelled as a random volume distribution of water whose concentration time curve was modelled as a Gaussian. Research shows that collagen cross-linking increases linearly in time post infarction and plateaus during the maturation stage [14]. In our model, similar to the approach taken in Haddad & Samani, cross-linking was expressed as a multiplication factor to the Yeoh hyperelastic coefficients. This factor was increased linearly throughout the simulation to an upper bound found through optimization in [7]. Lastly, we found little information on the temporally variable percentages of myocytes and fibroblasts with only 1 fibroblast concentration curve in the literature [15]. Due to their mechanical similarity and little prognostic value, the percentage volume of both microconstituents were combined and average mechanical properties were used; completing the temporal profile of the volume percentages of the microconstituents.

The healing timeline was then discretized into 57 equally spaced time points from day 0 to 56 or 8-weeks post myocardial infarction. The composite material model was run using the volume percentages at each time point to find the corresponding stress-strain curve.

3.2.4   « Neural Network Training and Evaluation »

Using the stress-strain curves generated from the model at discrete time points, a network was built to predict a continuous-time profile of stress-strain data. It is a 3-layer perceptron which takes the normalized healing stage time as the input, and outputs the stress-strain curve.

A preliminary evaluation of the population neural network library for scar tissue was conducted. Uniaxial compressive test data from [16] at day 14 post infarction was input to an optimization solver with our neural network training with input time, and output stresses at uniformly spaced strains. The stress-strain data time point that best agreed with the experimental data predicted the approximate location along the healing path.

3.3 « Results »

The results for the Fermi-Dirac fit of the experimental collagen factor increase is shown in Fig. 3. The curve had an R-square and RMSE values of 0.98 and 0.65, respectively. The volume percentages of all micro constituents during infarct healing is shown in Fig 3-4.
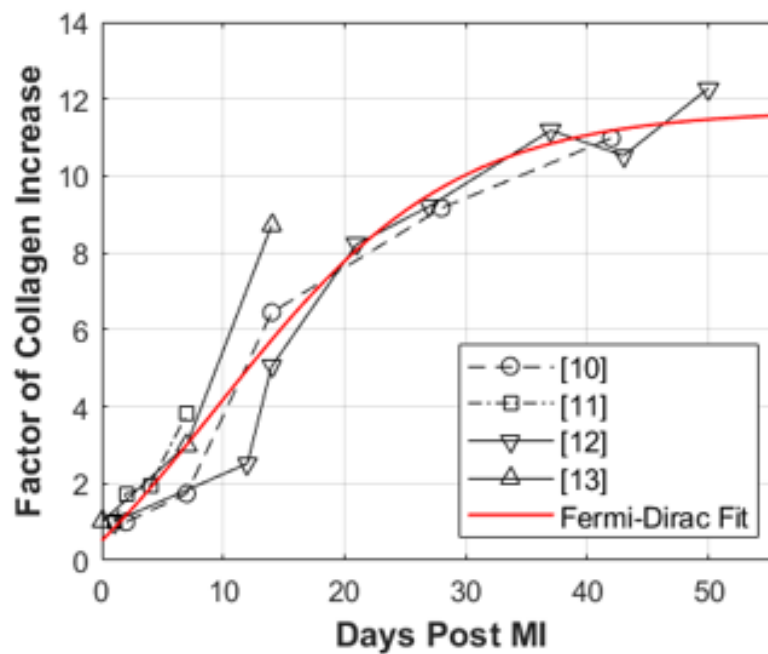
Figure 3-3 Collagen Fermi-Dirac factor function fit to experimental data from literature
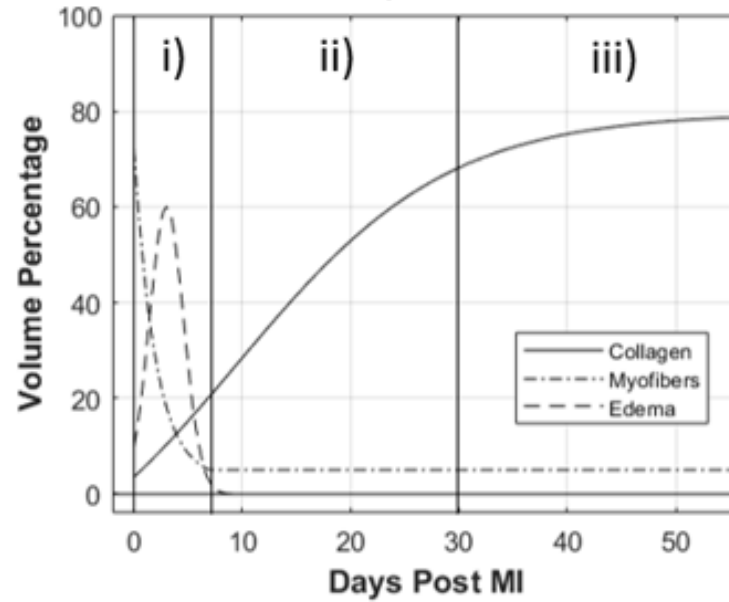
Figure 3-4 Volume percentage time course of healing scar tissue broken down into i) inflammatory stage, ii) proliferative stage, and iii) maturation stage.

The mechanical property results of those curves in the tissue model are presented in Fig 3-5 which shows a surface of the change in mechanical properties in times for tensile uniaxial testing of healing scar tissue.
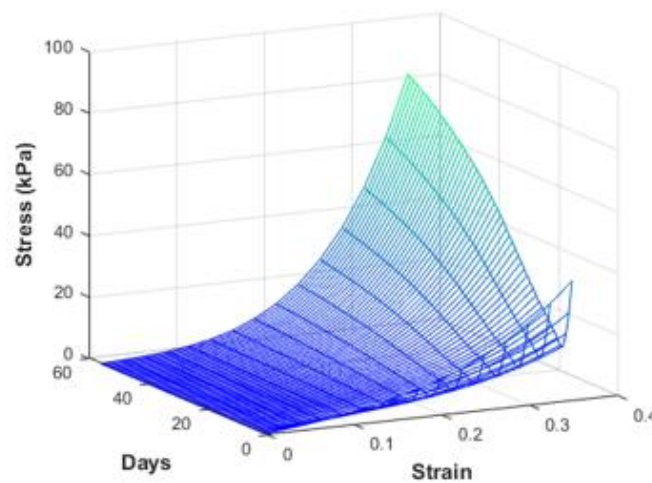
Figure 3-5 Mechanical property surface throughout the healing stage of scar tissue.

The day 14 uniaxial test data from [16] resulted in an optimized day of 19.1 predicted from our trained neural network giving an error of 5.1 days. Our model also predicts a 48.6% collagen composition, 5% myofiber density, and 46.4% combined fibroblast and myocyte tissue volume percentage.

3.4 « Discussion »

Beginning most importantly with the collagen increase factor function; from 4 separate labs, the data agreed quite well which motivated the fit. Although other functions could be considered for this fitting, the Fermi-Dirac was chosen due to its strict plateauing feature. Most importantly, is that from a fit obtained from 4 different result sets, an experimentally proven increase from a low volume of healthy collagen concentration to approximately 80% was captured as shown in Fig. 2b) [7]. The form of the curve also agrees well with the literature but is now quantitative instead of qualitative [11,17].

The preliminary evaluation of the population neural network library is promising. Day 14 uniaxial test data returned an estimated 19.1 days from our network. The prognostic significance of 5.1 days error is unknown at this stage in the study, but what can be highlighted is that both days 14 and 19.1 represent early stages of the proliferative phase. There also wasn't enough uniaxial test data on healing scar in the literature to give statistical power to the error. There are improvements that can also be made to the current methodology which will reduce this error. The coefficient for crosslinking used here was based off an ad-hoc approximation from 1 study of myocardial tissue stress-strain data [7]. By incorporating more results into the estimation, a more accurate and population-based estimate can be achieved.

There are 3 main limitations in this study. The collagen factor function does not accurately model collagen breakdown during the inflammatory stage where the literature reports ~25% decrease from healthy concentration in the first 2 days [17]. The form factor function also acts as an absolute function whereas, realistically, the final concentration of collagen in each patient will be different. To address this limitation, the network can be modified to be a 2-variable neural network. Lastly, while reasonably

realistic, the functions for the edema and myofiber constituents were not based on experimental data like the collagen function.

3.5   « Conclusions and Future Work »

For accurate cardiac biomechanical models used to study myocardial infarction, it is important to personalize the mechanical properties of the infarct region via inverse optimization. We proposed here the feasibility of a mechanical property library based on a micro-to-macro finite element simulation and compiled literature on the constituents of cardiac tissue previously published. This function can be incorporated in a model optimization algorithm based on cardiac imaging data (e.g. shape or displacement field) to stage the healing of scar tissue based on its predicted time point and predict the constituent compositions which may be used as effective prognostic biomarkers for rupture and healing rate.

Future work will be devoted to more accurate cross-linking simulation, and multiple models (plane, shear, and biaxial). The stress-strain curves from each model will be used to generate a network that will predict the Holzapfel-Ogden parameters during scar healing. These networks can then be evaluated with the extensive literature available to complement the uniaxial case for infarct tissue mechanical properties presented in this study.

« References »

[1]   Benjamin, E. J., Virani, S. S., Callaway, C. W., Chamberlain, A. M., Chang, A. R., Cheng, S., … Muntner, P. (2018). Heart disease and stroke statistics - 2018 update: A report from the American Heart Association. In *Circulation* (Vol. 137).

[2]   Sanchis-Gomar, F., Perez-Quilis, C., Leischik, R., & Lucia, A. (2016). Epidemiology of coronary heart disease and acute coronary syndrome. *Annals of Translational Medicine*, *4*(13), 256–256.

[3]   Nordsletten, D. A., Niederer, S. A., Nash, M. P., Hunter, P. J., & Smith, N. P. (2011). Coupling multi-physics models to cardiac mechanics. *Progress in Biophysics and Molecular Biology*, *104*(1–3), 77–88.

[4]   Liehn, E. A., Postea, O., Curaj, A., & Marx, N. (2011). Repair after myocardial infarction, between fantasy and reality: The role of chemokines. *Journal of the American College of Cardiology*, *58*(23), 2357–2362.

[5]   Holzapfel, G. A., & Ogden, R. W. (2009). Constitutive modelling of passive myocardium: A structurally based framework for material characterization. *Philosophical Transactions of the Royal Society A: Mathematical, Physical and Engineering Sciences*, *367*(1902), 3445–3475.

[6]   Balaban, G., Finsberg, H., Funke, S., Håland, T. F., Hopp, E., Sundnes, J., … Rognes, M. E. (2018). In vivo estimation of elastic heterogeneity in an infarcted human heart. *Biomechanics and Modeling in Mechanobiology*, *17*(5), 1317–1329.

[7]   Haddad, S. M. H., & Samani, A. (2017). A novel micro-to-macro approach for cardiac tissue mechanics. *Computer Methods in Biomechanics and Biomedical Engineering*, *20*(2), 215–229.

[8]   Holmes, J. W., Borg, T. K., & Covell, J. W. (2005). Structure and Mechanics of Healing Myocardial Infarcts. *Annual Reviews of Biomedical Engineering*.

[9]   Richardson, W. J., Clarke, S. A., Quinn, T. A., & Holmes, T. W. (2015). Physiological Implications of Myocardial Scar Structure. *Comprehensive Physiology*, *5*(4), 139–148.

[10]   Jugdutt, B. I., & Amy, R. W. M. (1986). Healing After Myocardial Infarction in the Dog : Changes in Infarct Hydroxyproline and Topography. *Journal of the American College of Cardiology*, *7*(1), 91–102.

[11]   Carlyle, W. C., Jacobson, A. W., Judd, D. L., Tian, B., Chu, C., Hauer, K. M., … Mcdonald, K. M. (1997). Delayed Reperfusion Alters Matrix Metalloproteinase Activity and Fibronectin mRNA Expression in the Infarct Zone of the Ligated Rat Heart. *Journal of Molecular and Cellular Cardiology*, *29*, 2451–2463.

[12]   Jugdutt, B., Joljart, M., Khan, M. (1996). Rate of Collagen Deposition During Healing and Ventricular Remodeling After Myocardial Infarction in Rat and Dog Models. *Circulation*,94,94-101

[13]   Cleutjens, J. P. M., Verluyten, M. J. A., Smits, J. F. M., & Daemen, M. J. A. P. (1995). Collagen Remodeling after Myocardial Infarction in the Rat Heart. *American Journal of Pathology*, *147*(2), 325–338.

[14]   Fomovsky, G. M., & Holmes, J. W. (2010). Evolution of scar structure , mechanics , and ventricular function after myocardial infarction in the rat. *American Journal of Physiology-Heart and Circulatory Physiology*, *298*, 221–228.

[15]   Yang, F., Liu, Y., Yang, X., Xu, J., Kapke, A., & Carretero, O. A. (2002). Myocardial infarction and cardiac remodelling in mice. *Experimental Physiology*, *87*(5), 547–555.

[16]   Sirry, M. S., Butler, J. R., Patnaik, S. S., Brazile, B., Bertucci, R., Claude, A., … Franz, T. (2016). Characterisation of the mechanical properties of infarcted myocardium in the rat under biaxial tension and uniaxial compression. *Journal of the Mechanical Behavior of Biomedical Materials*, *63*, 252–264.

[17]   Clarke, S. A., Richardson, W. J., & Holmes, J. W. (2016). Journal of Molecular and Cellular Cardiology Modifying the mechanics of healing infarcts : Is better the enemy of good ? *Journal of Molecular and Cellular Cardiology*, *93*, 115–124.

Chapter 4

4 « Effect of Cardiac Phase on CT Measured Cardiac Output in Healthy and Myocardial Infarcted Swine »

4.1 « Introduction »

Cardiac Output (CO) is an important clinical measurement that can aide in the diagnosis and prognosis of patients, as well as serve to validate models discussed in Chapter 2. A high CO can indicate sepsis in patients whereas a low CO may indicate cardiac dysfunction caused by cardiovascular disease (CVD) [1,2]. It is critical for haemodynamic monitoring intraoperatively, and perioperatively, where it is used to calculate oxygen delivery. This measurement can be used in goal-directed therapy via optimization of CO which has shown to reduce postoperative mortality and morbidity, as well as improved patient outcome [3-6].

Several opportunities exist during a patient's stay to calculate CO. In the diagnosis of coronary artery disease, dynamic contrast enhanced computed tomography (DCE-CT) imaging techniques are well established as a non-invasive evaluation [7]. While being able to measure the stenosis of the artery, DCE-CT also allows for myocardial perfusion imaging (MPI) to assess the functional damage caused by ischemia [8] and, can non-invasively measure CO without the need of further instrumentation or cost.

One area of DCE-CT imaging for myocardial perfusion that is up for contention is the optimal cardiac phase to trigger the imaging acquisition. While some labs trigger for end systole, where the myocardial wall is thicker providing more perfusion information, other labs trigger at mid-end diastole to minimize cardiac motion improving image reconstruction. It is currently unknown the effect this cardiac phase selection has on the additional CO measurement.

This paper examines the effect of reconstructed cardiac phase on the calculated CO in both healthy and myocardial infarcted pigs. Pigs were necessary as continuous collection of the cardiac cycle is required to reconstruct images at multiple cardiac phases; and with

dose considerations, was not possible in humans. Also reinvestigated is the equality of CO as measured by DCE-CT and manual segmentation.

4.2 « Methodology »

4.2.1 « Study Pool »

Seventeen porcine imaging data sets were used in this study. Table 4-1 shows the different pathological conditions of the subject prior to imaging. Myocardial infarction of the left anterior descending artery was induced as described in [8]. Some data sets during the healing time do come from the same pig, though since this is a study on DCE-CT in general, we did not consider this as significant.

Table 4-1 Pathological State of Porcine Subjects for Cardiac Imaging.

Condition of Subject	Number in Study
Healthy	4
1 Week Post Myocardial Infarction	4
4 Week Post Myocardial Infarction	4
8 Week Post Myocardial Infarction	5

4.2.2 « Scanning Protocol »

Each study included the pig being anesthetized and mechanically ventilated in a supine position on the scanner table, before a bolus of iodinated contrast (Isovue 370) was injected intravenously followed by saline flush. The volume of iodinated contrast was typically 0.7mL per kg of the patient. Next, a 30 s cine scan of the heart was acquired with breath-hold using a large-coverage CT scanner (GE Healthcare Revolution) at 100 kV voltage, 100 mA current and 280 ms gantry speed. The electrocardiogram of the pig was simultaneously recorded during the acquisition. DCE cardiac images were retrospectively reconstructed using filtered back projection at 30% to 80% of the R-R

intervals with a 5% phase increment. The in-plane resolution was 0.2x0.2mm and a slice thickness of 1.0mm.

4.2.3   « Cardiac Output »

4.2.3.1   « Calculating CO with DCE-CT »

CO was first reported measurable using dye dilution by G. N. Stewart in the late 1900's (9). Equation (1) which is now called the Stewart-Hamilton equation says the flow of blood in the body "Q", commonly in litres per minute, is measurable by sampling the concentration of an indicator in the blood stream in time and then dividing the mass "m" of the indicator by the integral of this sampled concentration time curve "$C_a(t)$".

$$Q = \frac{m}{\int C_a(t)dt} \qquad\qquad (1)$$

The indicator for DCE-CT is the Iodine used as contrast media in the imaging session. With electrocardiogram gating (ECG), the first pass of iodine concentration can be measured as collection is triggered providing the necessary $C_a(t)$ curve. This, along with the known volume and concentration of iodine allows us to calculate the mass of indicator needed in the SH equation completing the requirements to calculate CO.

4.2.3.2   « Cardiac Output Fitting »

Before taking the integral of $C_a(t)$, typically, an idealized curve is fit to the experimental curve $C_a(t)$. This reduces error caused by noise. Many approaches have been made to derive an equation for *C(t)* based on the physiology of the cardiovascular system. Some treated the function $C_a(t)$ as the convolution of some transfer function with a probability density function [10, 11]. Later, Thompson et. al. first suggested that the shape of $C_a(t)$ could be described by a modified gamma variate function (MGVF) given in equation 2 [12], this was an attractive model due to its relative simplicity. At the time, it simply happened to fit the curve well, and 20 years later it was derived from the physiological basis that the cardiovascular system was a series of mixing compartments [13]. Some labs have used lognormal curves to fit the function $C_a(t)$, however, the modified gamma

variate was chosen in the end due to its mass acceptance [14]. In this equation, K, α, and β are constants, AT is the "arrival time" of the contrast.

$$C_a(t) = K(t - AT)^\alpha e^{-(t-AT)/\beta} \quad\quad (2)$$

Before fitting the curve, the initial Hounsfield units of the blood pool needs to be subtracted from the curve seen in Figure 4-1, this ensures the signal measured comes from the iodine contrast alone. This step of translating the signal to baseline is not standardized and different labs may take different approaches such as averaging the first few points before the contrast washes in or using only the first point. To evaluate the difference between the two approaches for the baseline translation; the background blood pool was sampled at both the ascending aorta, as well as left ventricle and the HU's were compared. This was done for 5 of the imaging study data sets at phases 40%, 60%, and 80% phase of cardiac cycle reconstruction. A paired t-test was used to evaluate the similarity of either the first sampled HU point or the mean of first few before the wash-in of contrast with the sampled baseline HU of the left ventricle.

Based on the findings of results section 1, all subsequent CO estimates use only the first point to remove the blood signal. The MGVF curve C(t) was then fit using a least squares approach to the experimental data also removing the effect of recirculation by extrapolating the modified gamma variate fit to <1% of maximum amplitude.
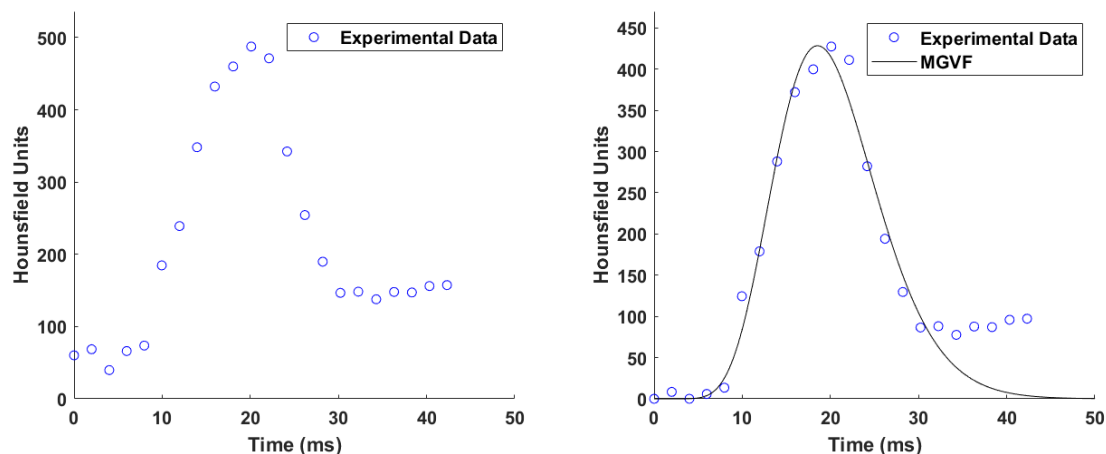
Figure 4-1. An example arterial enhancement concentration curve of Iodine in HU (left) and the MGV fit and extrapolation after normalization (right)

4.2.3.3 « Conversions and Sampling Location »

The location to sample the concentration does not matter in theory, and Ludman et. al. [15] shown that there was less than 2.5 % error when sampling from the left ventricle, ascending aorta, and descending aorta. The ascending aorta was ultimately chosen due to the more homogenous mixing of contrast than other locations while still having a large area to sample, minimizing photon noise. Because CT provides HU's, and concentration of contrast is required for the Stewart-Hamilton equation, it was necessary to convert HU into mg/mL. A previous study using the same scanner provides a conversion factor for concentration of Iodine and it's respective HU [16]. This was a linear conversion factor with no offset of 25 (HU/(mg/ml)) for 100kVp.

4.2.4 « Comparing the Effect of Phase »

The CO was calculated at each phase for each imaging session totalling 187 curves. The mean and standard deviation were taken over all phases for each data set to get an estimate of intrinsic error of picking a phase. Outside of the effect of phase, there are 2 dependant variables that can alter the estimated cardiac output; the mass of injector, and the integral in the denominator which we call the area under the curve (AUC). Since the mass of indicator has relatively little error as the concentration and volume are very

exact, most variability comes from the AUC's. The variability of these with phase are also calculated to see their effect on CO variability.

To see if there was any effect from the state of the pig heart post myocardial infarction, we also separated each pig by health, and compared the CO errors for the select phases of 40%, 60% and 80%.

4.2.5 « Manual Segmentation Comparison »

The CO as predicted from DCE-CT was also compared to the manual estimation calculated from segmentation of blood pool volumes and estimating cardiac output as heart rate times stroke volume which is end diastolic volume (EDV) minus end systolic volume (ESV) as shown in equation (3).

$$CO = (EDV - ESV) * HR \qquad (3)$$

Previously, [15] compared the agreement between DCE predicted cardiac output and manual and concluded they were not similar with a standard deviation between the two of 1.22L/min. This experiment was done on scanners that are now out of circulation, so we re-examined this study with the new state of the art scanner. To measure EDV and ESV, the blood pool of the CT images were manually delineated in 3D Slicer at 80% and 30% of the R-R interval representing the ED and ES states of the heart [17]. The blood was first threshold segmented, and then the papillary muscles was manually segmented to be included in the volume calculation. The delineation of blood from atrium to ventricle at the atrioventricular junction was chosen as planar cut at the mitral valve visible in both ED and ES. A similar planar cut was used at the aortic valve.

We ran a standard t-test to compare the similarity between both the manual and DCE predicted CO's.

4.3 « Results »

4.3.1 « Cardiac Output Fitting »

The paired t-test for both the single point baseline and mean point baseline when sampled from the ascending aorta were both nonsignificant with p-values of 0.67 and 0.45 when compared with the ventricle values. The mean sum of squared error (MSSE) using the single baseline point to the ventricle was 25.7 HU squared vs 40.9 HU squared using the mean, which suggests that the first baseline point is more representative of the true background HU value vs the mean baseline. The qualitative effect of averaging the first few baseline points vs just the non-contrast initial point is shown below in Figure 4-2. The quantitative effect on CO is shown in the bottom row of the figure for an example case. We noticed that using the first point as the baseline reduced error across phases for all studies.
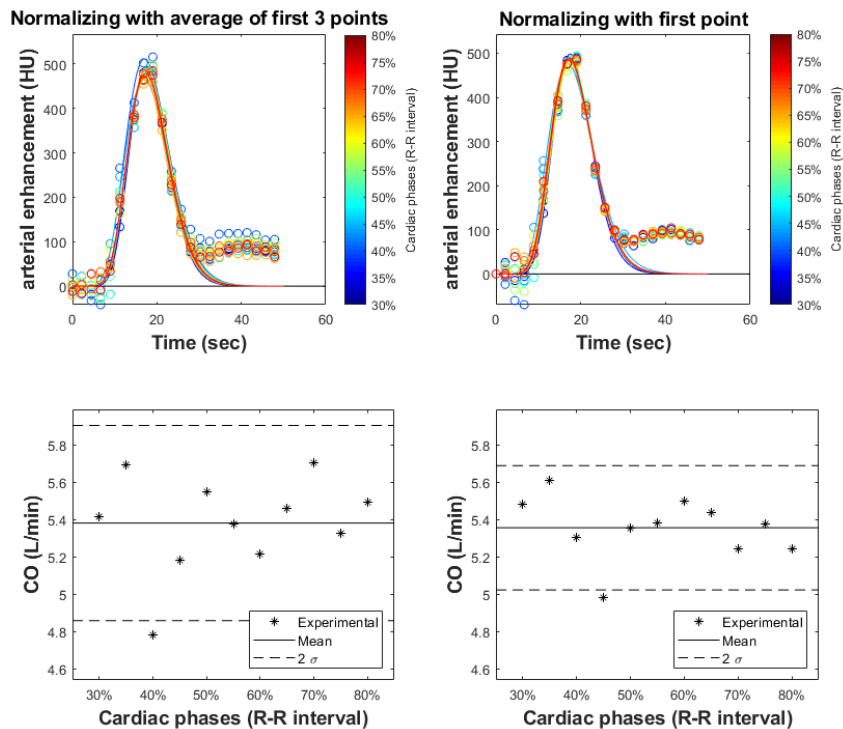

Figure 4-2 Effect of averaging the first few baseline points (left) and using just the non-contrast point (right) for removing blood signal and subsequent effect on CO estimation (below).

4.3.2 « CO using DCE as a Function of Cardiac Phase »

Figure 4-3 shows the variation of cardiac output values at all phases for all 17 pig studies. Due to the proposed protocol of only using the first data point to remove the effect of blood, and robustness of MGV fitting shown above, there are no obvious trends in CO prediction as we move from ES to ED. Since the major determinant in CO is the AUC, we also plot these values. Again, no trends exist amongst phase. The mean standard deviation of CO due to phase selection is 0.127L/min. The deviation of these measurements was approximately 40% compared to the mean. This contrasts the standard deviation of the AUC's with respect to phase which was 30% compared to the mean STD.
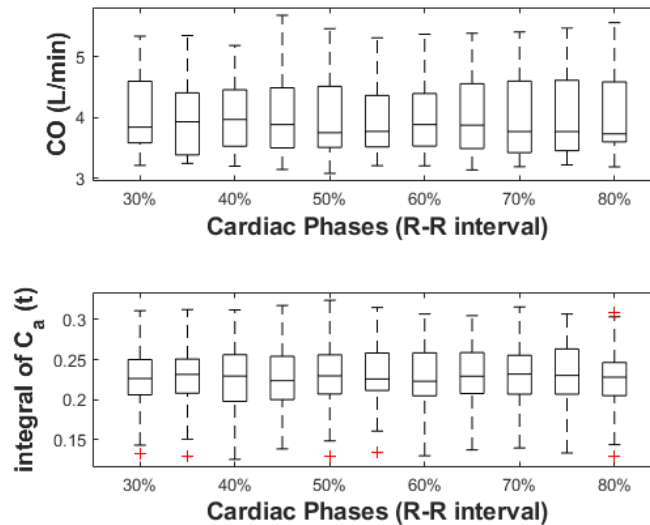
Figure 4-3 Cardiac Output predictions for all subjects at all phases (top) and AUC's for all subjects at all phases (bottom).

Figure 4-4 shows the CO variability for 3 phases separated by state of heart health. If there is no effect on heart health, it is expected that the estimates remain relatively constant at each phase as observed above.
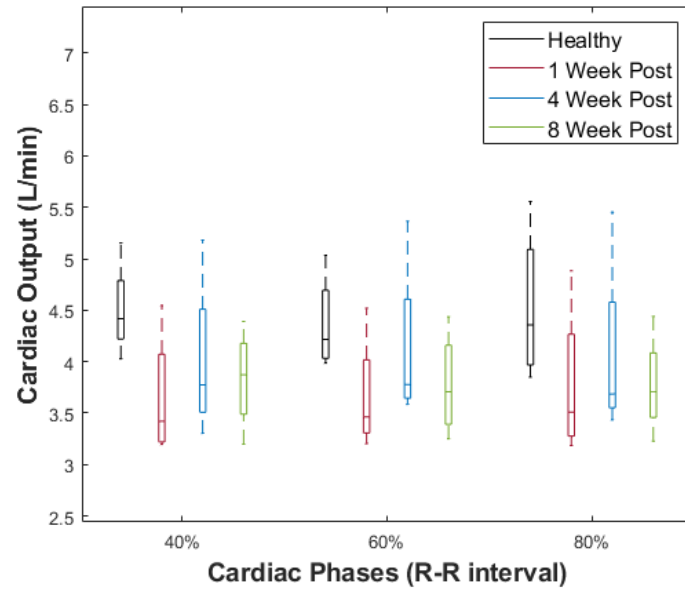
Figure 4-4 Influence of state of infarct healing and cardiac output as a function of phase for 40%, 60% and 80%.

4.3.3 « Comparison of CO Measurements from DCE and Manual Segmentation »

First included are example segmentations of the blood pool for end diastole and end systole shown in figure 4-5.
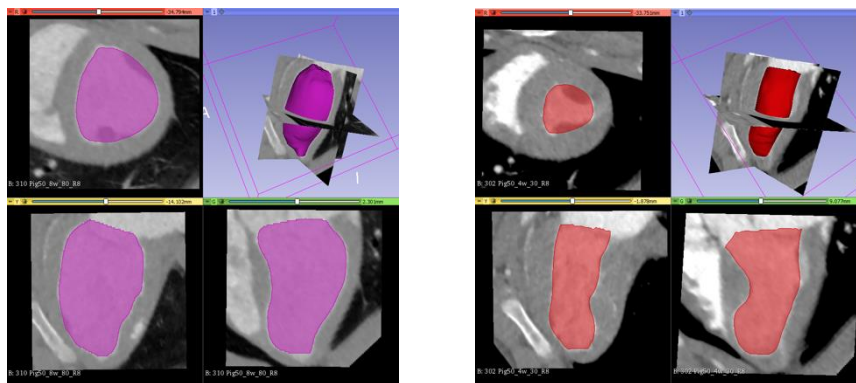
Figure 4-5 Example segmentations of the LV blood pool at ED (left) and ES (right).

The manual estimate of CO and estimate from indicator dilution theory were shown to be significantly different with a p-value less than <0.0001. The manually estimated CO was lower than indicator dilution estimated CO with a mean difference between estimates 0.94L/min ±0.72L/min shown in Figure 4-6.
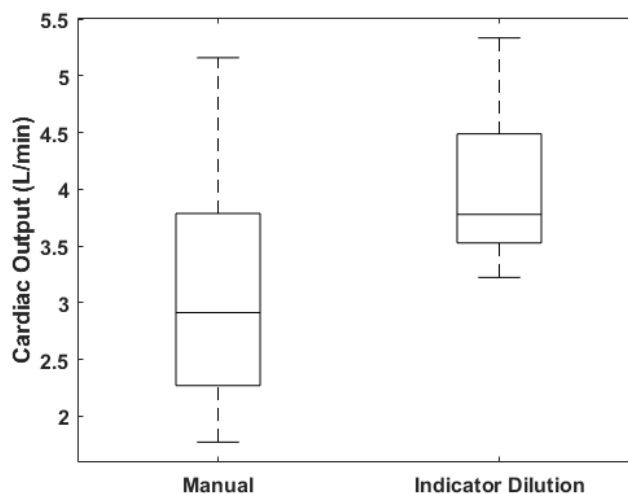
Figure 4-6 Comparison of manual vs indicator dilution CO's.

4.4 « Discussion »

4.4.1 « Cardiac Output Fitting »

From inspection of Figure 4-3, the effect of averaging the first few points have increased the disagreement between all experimental curves, this leads to larger variability in the AUC's which shows in the predicted cardiac outputs. Using only the first sampled point was shown to be better when comparing the MSSE of both methods and greatly reduce the variability in CO which leads to a better estimate of the CO error. It's also important to note that the MGV fitting is quite robust to outliers seen on the right side of Figure 4-3 where, though large variability near ES is still seen, the resulting fits are still quite close. This shows that a big factor when estimating CO is the first step of blood signal removal.

As for the cause of this variability; when the contrast is entering the heart, the disagreement seen in the wash-in stage in the ascending aorta is in fact caused by motion artifacts. As the bolus of iodine contrast travels towards the heart, it acts as a bright object

moving through the body. This motion creates artefacts in the form of hyper and hypo-enhancement streaks as visible in Figure 4-7 which affects the region of interest when sampling the average HU. Near systole, when the myocardium is also moving, the effects of this motion are exacerbated leading to larger discrepancies in HU prediction. There may also be influences from photon noise and beam hardening as well.
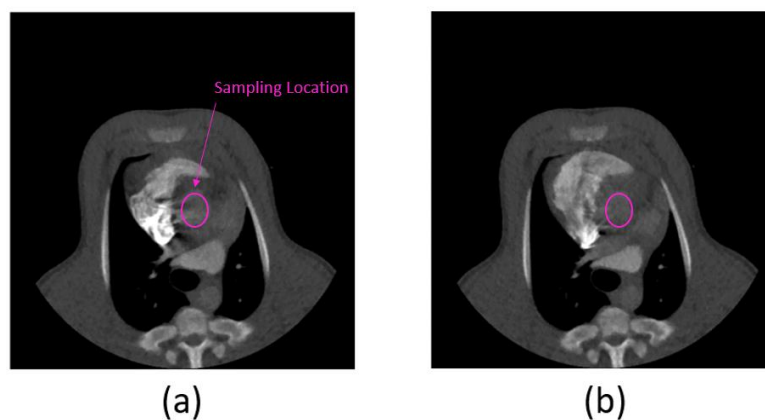
Figure 4-7 Artifacts caused during CT reconstruction with ES shown in a), and ED shown in b).

4.4.2   « Cardiac Phase »

There was no phase dependency on calculated cardiac output via indicator dilution methods with different phases of reconstruction. The CO as measured by DCE was highly reproducible across the 30%-80% R-R interval range where clinical cardiac studies are triggered. There was an intrinsic phase error that should be considered when reporting CO values with DCE-CT which is 0.128L/min. It's interesting to note that the AUC error was smaller than the error of the CO value itself. This shows that though the AUC is more stable, after using it in the SH equation, the error gets amplified due to it residing in the denominator. The cause of error amplification in CO is due to the overall magnitude range of cardiac output. The increase in error when we examine cardiac output is due to the magnitude of the value. A large AUC will lead to a smaller CO due to their inverse proportionality, which leads to smaller variability. Whereas a small AUC, can lead to a larger CO prediction and amplified error. This observation holds when the CO is

predicted from the same subject since the mass of the indicator is presumably the same amount. As the mass changes, we introduce a new variable which changes this trend.

The reproducibility of CO at different timepoints post infarction was not influenced. This is important since mechanically speaking a damaged heart produces more irregular mixing which may have led to poor sampling. Based on sampling at the ascending aorta, this showed no influence across phases.

4.4.3 « Manual CO Comparison»

There was a discrepancy between manually predicted CO, and CO predicted by indicator dilution having a mean difference of 0.94L/min ±0.72L/min. This contrasts Ludman's work where the mean value was 0.079 ±1.22L/min. There are two discussion points about the disagreement of findings relating to this previous study.

First, in [15], the slice thickness was 1cm vs our 2.5mm interpolated to 1mm. It's likely that with such few slices in [15], the LV volumes were overestimated which made the mean zero. With new scanner accuracy, our findings suggest that there is a bias of 0.94 L/min between both methods. However, the amount of data required to reconstruct a CT image is hard set. This makes capturing the heart at ES near impossible given the time the heart is fully contracted. It's likely the data at ES is overlapped with systolic contraction and start diastole. These influences make it difficult to delineate the true LV blood pool wall and likely always lead to overestimations of the ESV, reducing manual CO estimates. If the true volume was possible, presumably that bias would decrease to zero. To note, it's likely all newer scanners would maintain this bias; a unitless conversion factor from manual to DCE-CT may close the gap between both methods.

Second, we note that our manual to DCE-CT difference standard deviations have dropped [15] by 0.5L/min. Of course, this can never drop to zero given the intrinsic limitations in CT, and manually delineating the blood pool CT images. For instance, inter/intraobserver error, and incorrect triggering due to heart rate variability of the patient during imaging. This is encouraging as with newer technology; we are reaching a closer agreement between the two methods.

4.5   « Conclusions »

The accuracy of CO in the clinic can be vital to patient care and treatment. We examined the effect of cardiac phase reconstruction when CO is predicted using DCE-CT in healthy and infarcted myocardial swine. We noted no phase dependence on CO in either healthy or infarcted swine, there was however an intrinsic phase error of 0.128L/min. Due to the nature of the Stewart-Hamilton equation, and error of CO using this equation, we note that larger CO values have a larger error which may be useful when interpreting results from DCE-CT.

Towards a more standardized protocol for measuring CO using CT: Only the initial point should be used to remove the HU caused by blood. Subsequent points that may appear as "noise" are in fact motion artifacts affecting intensity caused by the movement of a bright bolus of contrast into the image plane.

Lastly, we note that the gap is closing between the agreement of manually estimated cardiac output, and indicator dilution methods in CT.

« References »

1.   Vincent, J. L. (2008). Understanding cardiac output. *Critical Care*, *12*(4), 12–14.

2.   https://www.ncbi.nlm.nih.gov/books/NBK470455/

3.   Saugel, B., Cecconi, M., Wagner, J. Y., & Reuter, D. A. (2015). Noninvasive continuous cardiac output monitoring in perioperative and intensive care medicine. *British Journal of Anaesthesia*, *114*(4), 562–575.

4.   Grocott, M. P. W., Dushianthan, A., Hamilton, M. A., Mythen, M. G., Harrison, D., & Rowan, K. (2013). Perioperative increase in global blood flow to explicit defined goals and outcomes after surgery: A cochrane systematic review. *British Journal of Anaesthesia*, *111*(4), 535–548.

5.   Cecconi, M., Corredor, C., Arulkumaran, N., Abuella, G., Ball, J., Grounds, R. M., … Rhodes, A. (2013). Clinical review: Goal-directed therapy-what is the evidence in surgical patients? The effect on different risk groups. *Critical Care (London, England)*, *17*(2), 209.

6.   Lilot, M., Bellon, A., Gueugnon, M., Laplace, M. C., Baffeleuf, B., Hacquard, P., … Piriou, V. (2018). Comparison of cardiac output optimization with an automated closed-loop goal-directed fluid therapy versus non standardized manual fluid administration during elective abdominal surgery: first prospective randomized controlled trial. *Journal of Clinical Monitoring and Computing*, *32*(6), 993–1003.

7.   Varga-Szemes, A., Meinel, F. G., De Cecco, C. N., Fuller, S. R., Bayer, R. R., & Joseph Schoepf, U. (2015). CT Myocardial Perfusion Imaging. *American Journal of Roentgenology*, *204*(3), 487–497.

8.   So, A., Wisenberg, G., Teefy, P., Yadegari, A., Bagur, R., Hadway, J., … Lee, T. Y. (2018). Functional CT assessment of extravascular contrast distribution volume and myocardial perfusion in acute myocardial infarction. *International Journal of Cardiology*, *266*, 15–23.

9.   Stewart, G. N. (1891). Researches on the Circulation Time and on the Influences Which Affect it. *American Journal of Physiology*.

10.   Zierler, K. (2000). Indicator dilution methods for measuring blood flow, volume, and other properties of biological systems: a brief history and memoir. *Annals of Biomedical Engineering*, *28*(8), 836–848.

11.   Stephenson, J. L. (1958). Theory of Measurement of Blood Flow by Dye Dilution Technique. *IRE Transactions on Medical Electronics*, *PGME-12*, 82–88.

12.   THOMPSON, H. K., STARMER, C. F., WHALEN, R. E., & MCINTOSH, H. D. (1964). Indicator Transit Time Considered as a Gamma Variate. *Circulation Research*, *14*(6), 502–515.

13.   Davenport, R. (1983). The Derivation of the Gamma-Variate Relationship for Tracer Dilution Curves, *24*(10), 945–949.

14.   Band, D. M., Linton, R. A. F., O'Brien, T. K., Jonas, M. M., & Linton, N. W. F. (1997). The shape of indicator dilution curves used for cardiac output measurement in man. *Journal of Physiology*, *498*(1), 225–229.

15.   Ludman, P. F., Coats, A. J. S., Poole-Wilson, P. A., & Rees, R. S. O. (1993). Measurement accuracy of cardiac output in humans: Indicator-dilution technique versus geometric analysis by ultrafast computed tomography. *Journal of the American College of Cardiology*, *21*(6), 1482–1489.

16.   So, A., Imai, Y., Nett, B., Jackson, J., Nett, L., Hsieh, J., … Lee, T. Y. (2016). Technical Note: Evaluation of a 160-mm/256-row CT scanner for whole-heart quantitative myocardial perfusion imaging. *Medical Physics*, *43*(8), 4821–4832.

17.   3D Slicer. http://www.slicer.org. Accessed May 1st, 2018

Chapter 5

5 « Conclusions and Future Work »

5.1 « Conclusions »

In this thesis, techniques were presented to predict new non-invasive biomarkers, and risk factors for patients with myocardial infarction were developed using a biomechanical model of the left ventricle and cardiac tissue. Also investigated was when to calculate cardiac output which will be used as a validation metric in the future. The first technique was developed using a novel modeling approach to characterize myofiber contraction through estimating contraction forces of both healthy and different types of damaged cardiac tissue. The second developed technique utilized development of a library of scar cardiac tissue at various healing stages. It aimed at efficient determination of staging of scar healing and providing an estimate of collagen concentration in the tissue non-invasively. Lastly, to prepare this study for an in-vivo cardiac function assessment, accuracy of in-vivo validation technique to predict ejection fraction and cardiac output was conducted. This study revealed a necessity to change the methodology of state-of-the-art indicator dilution using contrast enhanced CT. Summaries with emphasis on application are provided below for Chapters 2, 3, and 4 of the thesis.

5.2 « Chapter 2 »

A novel method to predict contraction force variables in an acute myocardial infarct LV was developed. The method was developed based on an inverse problem framework where the LV model biomechanical model was used as the forward model. The inverse problem solution was founded on shape optimization where the biomechanical model is iteratively fed a set of contraction force parameters corresponding to healthy and ischemic cardiac tissue and resulting model shape is compared with the segmented shape obtained from medical imaging until the model and segmented LV shapes reach maximum similarity. As a proof of concept, the accuracy of this technique was evaluated using a 3-region heterogenous model. The contraction forces were reconstructed within errors of only 6%. These results are encouraging, hence justify developing a clinical study involving actual human or animal LV geometry. In the context of inverse problem

solution, forward biomechanical models are run tens or even thousands of times before a reliable solution can be found. As such, utilizing full biomechanical models are computationally expensive within such frameworks. To reduce the computation time, a reduced LV biomechanical model was developed using principal component analysis (PCA) in conjunction with neural network. The neural network was trained using data generated using full FE based LV models before applying PCA to reduce the FE solution dimensions which is necessary for training the network. To our knowledge this is the first neural network based reduced biomechanical model of the LV.

There are many benefits to the knowledge of contraction forces in the LV. They can define how damaged the myofibers are. An interesting feature in our model is the introduction of a contractility variable which represents the percentage of non-contracting fibers within ischemic tissue. These fibers may be either hibernating or necrotic which allows for a predictive healing range of the LV for clinical use. This chapter also offers the first technique of contraction force reconstruction that is CT compatible. This opens the possibility of this novel use of the CT imaging modality for cardiac mechanics assessment. Such assessment typically requires imaging modalities with tissue motions tracking capability (e.g. MRI).

5.3 « Chapter 3 »

During the healing stages post myocardial infarction, the mechanics of the infarct region are extremely important as they govern whether the LV will burst. The mechanics of infarct region also play a significant role in accurate patient-specific cardiac biomechanical modelling directly effecting stress predictions. Such modelling can become quite complex when tuning multivariable heterogenous mechanical properties to each patient. To simplify the tuning process while also providing value to the clinic. A scar tissue network which predicts the healing mechanical properties of scar was developed. This network was built from a micro constituent cardiac tissue model. We compiled all available literature to model the increase in collagen, cross-linking, myofibers and cells in time, and fed the single time variable to output LV tissue mechanical properties. Interesting to note, is that this model linked 6 separate studies together in a coherent understanding of collagen increase in infarcted tissue. A primary

test of our mechanical model to predict the stage of healing of infarct tissue was conducted with moderate accuracy. As discussed in the future work, this accuracy can be improved. The methodology introduced in this chapter offers a bridge between quantitative data of cardiac tissue microconstituents and tissue hyperelastic strain energy density functions.

5.4 « Chapter 4 »

Investigated was the effect of image reconstruction phase of cardiac output predicted by indicator dilution using DCE-CT. The primary use of this knowledge in relation to the thesis was to establish the correct measure of cardiac output which can predict ejection fraction in-vivo without using error prone segmentation. State of the art measurement techniques were used to collect the data on both healthy and infarcted pigs. While there was no dependence on phase or cardiac health, new information on error and novel relationships was found. Our results indicate that larger cardiac outputs from indicator dilution have more error than smaller ones. A relationship between heart rate and AUC was suggested based on the data obtained in the study. The findings in this chapter justify a study into this novel relationship aiming at developing a simple way for real-time estimation of cardiac output intraoperatively and perioperatively.

Also investigated and proposed, is a change to methodology for indicator dilution techniques. A necessary step is removing the background signal of the blood. We propose to only use the first sampled time point to remove the background as opposed to averaging which increased the error of estimated cardiac output and introduced interference caused by motion artifacts.

5.5 « Future Work »

In this thesis, techniques were presented to improve the predictive prognosis of patients who suffer from myocardial infarction. The techniques involve the definition of new variables that help quantify the damage, as well as state of healing of infarct tissue. Results obtained based on these developed techniques are encouraging and justify future study of in-vivo LVs that have follow up imaging sessions post myocardial infarction.

There, both techniques introduced in Chapters 2 and 3 could be used in the early imaging to define the damage, and then compared with the state of the healed left ventricle later.

5.5.1 « Left Ventricle Improvements »

The left ventricle model can be improved in several ways. The activation of myofiber contraction in the model is currently set to reach its maximum contraction linearly which only allows it to agree with the end systolic state. While in Chapter 2, this proved to be enough to characterize the damage, if more phases of the cardiac cycle are used (for instance in MRI where ionizing energy is not a concern); modelling the fiber contraction to match physiological force-time curves would allow multiple phases to be used in the shape optimization technique and likely improve accuracy.

Due to image artifacts, damaged cardiac tissue as visualized in medical images may not be the true geometric representation of the damaged region. A study into shape perturbation functions to change the geometry of the damaged region in question should be done. If a modified geometry shows a better fit to the cardiac motion and shape, it may suggest that the modified geometry represents a better estimate of the tissue extent of damage. A study to increase the heterogeneity of the LV is also warranted.

To obtain accurate stresses and contraction forces in the LV tissue it is important to use the LV reference geometry which corresponds to stress-free condition. This is commonly done by using invasive catheterization to measure the pressure in the heart, and within an inverse problem formula, determine the unloaded geometry that best agrees with the loaded pressure post deformation. This catherization is costly and associated with health risks, hence it could be replaced by a non-invasive inverse problem-based technique. The proposed technique involves computational assessment of the LV shape throughout the diastolic cycle after dimension reduction using PCA. This dimension reduction makes possible using extrapolation to obtain the unloaded LV geometry.

5.5.2 « Scar network improvements »

Currently, the scar model presents a uniaxial test simulation. This alone would not suffice to define cardiac tissue which typically presents in a simplified manner as transverse

isotropic. As discussed in Chapter 3, different simulations of biaxial, plane and shear tests should also be carried out to fully characterize healing tissue and compared with the literature. The concept of this network should also be used to study cardiomyopathy where the left ventricle stiffens over time. If a network that goes from healthy tissue, to progressively stiffer by increasing collagen and cross-linking, this stiffness increase information may be used in the clinic as an early sign of heart failure due to remote remodelling of cardiac tissue.

Curriculum Vitae

Name: Sergio C. H. Dempsey

Post-secondary   Western University
Education and   London, Ontario, Canada
Degrees: 2014-2018 H.B.Sc.(Medical Physics)

                              Western University
                              London, Ontario, Canada
                              2018-2020 M.E.Sc. (Biomedical Engineering)

Honours and   Western Graduate Research Scholarship
Awards: Western University, London, ON, Canada
                              2018-2020

                              John Hart Hunter Educational Foundation Award
                              Lansing, NY, United States of America
                              2017

                              Natural Sciences and Engineering Research Council of Canada
                              Undergraduate Student Research Award
                              2017

                              Best Poster Award Physics Undergraduate Conference
                              Western University, London, ON, Canada
                              2017

Related Work   Teaching Assistant
Experience   Western University
                              2016-2020

                              Undergraduate/Graduate Research Assistant in Physics
                              Western University
                              2016-2020

Publications:

Submitted Journal Papers:

Dempsey, S., So, A., Samani, A., (2020) "Characterizing Regional Myofiber Damage Post-Acute Myocardial Infarction Using Shape Optimization". International Journal of engineering Sciences.

Dempsey, S., Samani, A., So, A., (2020) "Effect of Cardiac Phase on CT Measured Cardiac Output in Healthy and Myocardial Infarcted Swine". European Radiology.

Conference Publications:

Miranda D., Jafari P., **Dempsey, S.**, Samani, A., (2020) "4D-CT Hyper-Elastography Using a Biomechanical Model". EMBC, Annual International Conference of the IEEE Engineering in Medicine and Biology Society. IEEE, [Accepted].

Dempsey, S., So, A., Samani, A., (2020) "A Composite Material Technique to Stage Scar Tissue and Predict Mechanical Properties". Annual International Conference of the IEEE Engineering in Medicine and Biology Society. IEEE, [Accepted].

Dempsey, S., So, A., Samani, A., (2019) "A Shape Optimization Technique to Predict Left Ventricle Ischemic Tissue Damage". 2019 Annual International Conference of the IEEE Engineering in Medicine and Biology Society. IEEE, 2019.

Dempsey, S., Samani, A., (2018) "Determining in-silico left ventricular contraction force of myocardial infarct tissue using a composite material model". Medical Imaging 2018: Image-Guided Procedures, Robotic Interventions, and Modeling.

Oral Presentations:

Dempsey, S., So, A., Samani, A., "Characterizing Regional Myofiber Damage Post-Acute Myocardial Infarction Using Shape Optimization". In 41st Engineering in Medicine and Biology Conference, Berlin, Germany. July 2019.

Dempsey, S., Samani, A., So, A., "effect of phase.. LHRD", In London Health Research Day (LHRD), London, ON. May 2019.

Dempsey, S., Samani, A., "Determining in-silico left ventricular contraction force of myocardial infarct tissue using a composite material model". Medical Imaging 2018: Image-Guided Procedures, Robotic Interventions, and Modeling. March 2018.

Poster Presentations:

Dempsey, S., Samani, A., "Determining Left Ventricular Contraction Force of Myocardial Ischemic Tissue", In London Health Research Day (LHRD), London, ON. May 2017.

Dempsey, S., Hocking, W., "Spectral Analysis of Buoyancy waves in the Troposphere", In Physics Undergraduate Conference (PhUnC), London, ON. March 2017.